

**Cell Reports Physical Science, Volume 4**

**Supplemental information**

**SARS-CoV-2 evolved variants**

**optimize binding to cellular glyocalyx**

**Sang Hoon Kim, Fiona L. Kearns, Mia A. Rosenfeld, Lane Votapka, Lorenzo Casalino, Micah Papanikolas, Rommie E. Amaro, and Ronit Freeman**

## Table of Contents:

### 1. List of Abbreviations

### 2. Supplemental Experimental Procedures:

#### 2.1 Computational Methods

- 2.1.1 WT, Delta, Omicron Spike System Construction, MD Simulation, and Clustering
- 2.1.2 Ensemble-based Docking with AutoDock Vina
- 2.1.3 Schrodinger IFD
- 2.1.4 Brownian Dynamics Simulations
- 2.1.5 Spike RBD+ACE2 MD Simulations
- 2.1.6 Dynamical Electrostatic Potential Map Calculations

#### 2.2 Experimental Methods

- 2.2.1 Materials
- 2.2.2 Biotin conjugation to heparin
- 2.2.3 Immobilization and binding of heparin, ACE2 to variant spike proteins
- 2.2.4 Biolayer interferometry (BLI)
- 2.2.5 Checking ternary complex formation (Spike-HS-ACE2) using ELISA
- 2.2.6 Checking ternary complex formation (Spike-HS-ACE2) using Mass Photometer
- 2.2.7 Preparation of signaling probes for GlycoGrip
- 2.2.8 Preparation of GlycoGrip LFSA
- 2.2.9 Comparison of the variant detection in GlycoGrip 1.0 and GlycoGrip 2.0
- 2.2.10 Evaluation of Selectivity and sensitivity of GlycoGrip2.0
- 2.2.11 Signal enhancement analysis

#### 2.3 Results and Discussion:

- 2.3.1 Summary of AutoDock Vina Results
- 2.3.2 Summary of Schrödinger IFD Results

### 3. Schemes:

- Scheme S1: Schematic outlining variant spike simulation, clustering, and AutoDock Vina procedures as discussed in Computational Methods Sections 2.1.1 to 2.1.3.
- Scheme S2: Schrodinger IFD Methodology at pH 7.4

### 4. Table:

- **Table S1:** Complete list of all mutations per variant considered for modeling and charge calculations in this work.
- **Table S2:** Complete list of all titratable residues and their selected protonation states each spike/ACE2 structure to pH = 7.4 as calculated by PROPKA. Full pK<sub>a</sub> calculation data can be found in the shared files associated with this supporting information.
- **Table S3:** Complete list of residues per HEP binding hotspot
- **Table S4:** Fraction of each group measured by mass photometer for Omicron ternary complex with or without heparan sulfate.
- **Table S5:** Fraction of each group measured by mass photometer for Delta ternary complex with or without heparan sulfate.

- **Table S6:** Fraction of each group measured by mass photometer for WT ternary complex with or without heparan sulfate.
- **Table S7:** Comparison of the limit of detection for spike protein detection in lateral flow assay

## 5. Figures:

- **Figure S1:** BLI sensogram of the ACE2 binding to variant of SARS-CoV-2 spike proteins.
- **Figure S2:** Figure describing MD simulation results of RBD+ACE2 systems.
- **Figure S3:** BLI sensogram of the heparin binding to variant of SARS-CoV-2 spike proteins.
- **Figure S4:** AutoDock Vina docking results illustrating heparin dimeric and tetrameric models bound to WT (A) closed and (B) 1-up structures.
- **Figure S5:** AutoDock Vina docking results illustrating heparin dimeric and tetrameric models bound to Delta (A) closed and (B) 1-up structures.
- **Figure S6:** AutoDock Vina docking results illustrating heparin dimeric and tetrameric models bound to Omicron (A) closed and (B) 1-up structures.
- **Figure S7:** K-means clustering results determining the optimal number of clusters from 28,800 AutoDock vina binding modes.
- **Figure S8:** All 19 heparin hotspots found via ensemble-based docking with AutoDock and kmeans clustering.
- **Figure S9:** Accessible Surface Area plotted for each site calculated with a probe radius of 7.2Å, calculated according to the Shrake-Rupley algorithm.
- **Figure S10:** Violin plots demonstrating distribution of AutoDock Vina binding scores for heparin dimer (hep2) and tetramer (hep4) models each binding hotspot across all variants.
- **Figure S11:** Violin plots demonstrating distribution of AutoDock Vina binding scores for heparin dimer (hep2) and tetramer (hep4) models each binding hotspot across 1up and closed spike structures.
- **Figure S12:** Violin plots illustrating the distribution of binding scores predicted by Schrodinger's Induced Fit Docking protocol in each of the probed sites, for each of the Variants, at pH's 7.4.
- **Figure S13:** Dynamically-averaged electrostatic potential maps collected from 50 ns of MD simulations for (A) WT, (B) Delta, (C) Omicron spike proteins in the 1up RBD conformation, and (D) Images demonstrating co-bind of ACE2 and HEP to 1up SARS-CoV-2 Spike
- **Figure S14:** Repetition results of Omicron variant mass photometer. Row (A) Omicron spike + HS + ACE2, and row (B) Omicron spike + ACE2.
- **Figure S15:** Repetition results of Delta variant mass photometer. Row (A) Delta spike + HS + ACE2, and row (B) Delta spike + ACE2.
- **Figure S16:** Repetition results of Wild type mass photometer. Row (A) WT spike + HS + ACE2, and row (B) WT spike + ACE2.
- **Figure S17:** Dose-dependency results of Omicron detection using *GlycoGrip2.0* without signal enhancement. The limit of the detection was calculated by the blank + 3x (Standard deviation of blank).

- **Figure S18:** Dose-dependency results of Omicron detection using *GlycoGrip2.0* with signal enhancement. The limit of the detection was calculated by the blank + 3x (Standard deviation of blank). At least three independent tests were performed ( $n \geq 3$ ).
- **Figure S19:** ChemDraws of all molecules modeled and docked in this work. Hep2mer, hep4mer, h6s2mer, h6s4mer.
- **Figure S20:** Comparison of the heparin and heparan sulfate for mass photometer.

## 1. List of Abbreviations:

- VOC: Variant of Concern
- RBD: Receptor Binding Domain
- RBM: Receptor Binding Motif
- FCS: Furin Cleavage Site
- 1up: shorthand describing when one spike RBD is in the “up”/“open” state
- ACE2: Angiotensin Converting Enzyme 2
- TMPRSS2: Transmembrane Serine Protease 2
- GAGs: GlycosAminoGlycans
- HEP: Heparin
- HS: Heparan Sulfate
- ESP: electrostatic potential
- BD: Brownian Dynamics
- MD: Molecular Dynamics
- IFD: Induced Fit Docking, particularly the flexible ligand-flexible receptor protocol provided by Schrodinger Suite of programs using Glide and Prime to model ligand and protein flexibility

## 2. Supplemental Experimental Procedures

### 2.1 Computational Methods:

#### 2.1.1. WT, Delta, Omicron Spike System Construction, MD Simulation, and Clustering:

Fully glycosylated, all-atom models of WT, Delta, and Omicron SARS-CoV-2 spike glycoprotein head domains (residues 13 to 1140) were constructed according to the following protocols.

*WT:* For construction of our WT “closed”/all RBD down system, a cryo-EM structure with 2.8 Å resolution was used (PDB ID 6VXX).<sup>1</sup> To improve the accuracy of our model, we incorporated fully resolved NTD, RBD, and pre-fusion loops from another closed spike structure (PDB ID 7JJI).<sup>2</sup> For construction of our WT “open”/1 RBD up system, a cryo-EM structure with 3.46 Å resolution was used (PDB ID 6VSB).<sup>3</sup> To improve the accuracy of our open model, we incorporated fully resolved RBD in an up-state bound to ACE2 (PDB ID 6M17)<sup>4</sup> and fully resolved NTD and pre-fusion loops (PDB ID 7JJI).<sup>2</sup>

*Delta:* We used the WT open and closed structures as described above as the basis for construction of our Delta variant closed and open spike glycoprotein systems. To account for the mutation profile in the Delta

variant, we induced single point mutations using the “mutate” command in psfgen. Experimental data showed significant rearrangement/structural remodeling of the NTD on Delta, so we incorporated a cryo-EM structure of the remodeled Delta variant NTD (PDB ID 7SO9).<sup>4</sup>

*Omicron:* For construction of our Omicron variant closed system, a cryo-EM structure with 3.36 Å resolution was used (PDB ID 7TF8)<sup>5</sup> as the base structure. Missing loops from the furin cleavage site in the Omicron PDB were grafted in from PDB ID 6VSB.<sup>3</sup> For construction of our Omicron variant open system, a cryo-EM structure with 3.40 Å resolution was used (PDB ID 7TEI)<sup>5</sup> as the base structure. Missing loops in the furin cleavage site, fusion peptide, and RBD were grafted in from PDB ID 6VSB.<sup>3</sup> For both open and closed omicron spike glycoprotein systems, we incorporated a cryo-EM structure of a fully resolved Omicron NTD (PDB ID 7K4N).<sup>6</sup>

*Glycosylation/ Protonation/ Solvation/ Neutralization:* All spike models were then glycosylated following the same glycoprofile as used by Casalino et al.,<sup>7</sup> consistent with Watanabe et al.<sup>8</sup> Protonation states were assigned by performing stand-alone PROPKA3<sup>9</sup> so that the glycan atoms were considered in the calculation, however protonation states (HSE vs HSD) for histidines were assigned by use of PROPKA through Schrödinger’s Protein Preparation Wizard tool.<sup>10</sup> AutoIMD, a VMD tool,<sup>11</sup> was used to resolve any glycan/protein clashes or ring penetrations in our glycoprotein systems. Glycoprotein models were then each solvated in explicit water boxes of 215 x 215 x 215 Å<sup>3</sup> and neutralized with 0.15 M NaCl.

*Molecular Dynamics Simulations:* All structures (6 models in total) were then subjected to the following Molecular Dynamics (MD) simulation protocol (1 replica each) with NAMD2.14,<sup>12,13</sup> all atoms described according to CHARMM36m all-atom force field:<sup>14-16</sup> 20,000 steps of Steepest Descent minimization for TIP3 water molecules and NaCl ions. Protein and glycan atoms were held fixed with a Lagrangian constraint. Heating of the solvated system from 10K to 310K by increments of 25K with protein and glycan atoms held in light restraint according to a force constant of 1 kcal/mol/Å. With each increase in temperature, 10080 steps (1fs/step) of MD simulation were performed within the NpT ensemble. Once the temperature reached 310K, 0.5 ns of NVT equilibration was performed with restraints maintained. NpT equilibration (310K, 1.01325 bar) for 0.5 ns (2fs/step) with restraint (force constant = 1 kcal/mol/Å) applied to all protein backbone atoms. Pressure was maintained a Langevin barostat. Box cell dimensions were set to flexible during pressure equilibration. NVT free (no restraints) production (310K, 1.01325 bar) simulations for 50 ns (2fs/step). 50ns NVT production runs were performed on TACC Frontera. As system pressure was equilibrated in the prior step, box cell flexibility was turned off in this step (useFlexibleCell = no).

*Clustering:* In preparation for ensemble-based spike/GAG docking studies with AutoDock Vina,<sup>17,18</sup> we selected the final frame of each 50ns MD simulation to serve as a rigid-docking receptor. We also clustered the 50ns trajectories to generate 5 other receptor structures per spike glycoprotein model. The 50ns trajectories were clustered in Python (with MDAnalysis<sup>19,20</sup> and Scikit-learn<sup>21</sup>) according to the following protocol: To remove global rotational and translational degrees of freedom before clustering, VMD<sup>11</sup> was used to align trajectories according to minimum Root Mean Square Deviation (RMSD) distance of all C<sub>α</sub> atoms from their first frame positions. Water and ion atoms were stripped from resultant aligned trajectories. Aligned trajectories were then opened as universes in MDAnalysis<sup>19,20</sup> wherein the RMSDs of C<sub>α</sub> atoms and glycan carbon atoms were calculated for each frame. Python Scikit-learn’s<sup>21</sup> Kmeans clustering package was then used to cluster all frames according to C<sub>α</sub> atom and glycan carbon atom RMSDs, and the knee locator algorithm was used to select the optimal number of clusters per simulation.

Representative structures -- i.e., those simulation frames closest in RMSD space from the true cluster center -- for the 5 most populated clusters were then selected for ensemble-based docking with AutoDock Vina.<sup>18,19</sup> PSF/PDB pairs were generated for each structure selected herein (i.e., for the final frame and for all clustered frames) and have been made available with our shared data sets on the AmaroLab website (<https://amarolab.ucsd.edu/covid19.php>).

### 2.1.2 Ensemble-based Docking with AutoDock Vina:

As described above, we selected 6 total structures per spike conformation (the final frame from 50ns and 5 representative structures from most populated clusters) to serve as receptors in ensemble based rigid docking studies with AutoDock Vina.<sup>17,18</sup> The following docking methods are detailed graphically in **Scheme S1** below. Each chosen spike receptor structure (3 variants x 2 conformational states x 6 selected frames = 36 total receptor structures) was subjected to the following protocol. To ensure receptor grids generated with AutoDockTools<sup>18</sup> would be similarly applied to each receptor structure, first all receptor PDB structures were aligned to one another according to the S2 domain C $\alpha$  atoms (protein residues 686 to 1140). After alignment, all receptor structures were converted to pdbqt filetype with AutoDockTools.<sup>18</sup> Heparin (HEP) dimer and tetramer .pdbqt structures were used in previous work<sup>18</sup> and thus the same files were used in this work (see **Figure S19** for images denoting exact molecular structures modeled in this work). Per protein structure, the center of the AutoDock<sup>13,14</sup> receptor grid was defined as the geometric center of the central helix atoms (protein residues 985 to 1000); this was a choice made to ensure relative consistency of the box center for all structures, regardless of closed/1up conformation. Grid box size was set to 150 x 150 x 150 Å<sup>3</sup> for all spike structures, this was chosen to ensure RBDs in the 1up state would still be encompassed within the resultant grid. All docking input files can be found in the datasets shared on the AmaroLab website (<https://amarolab.ucsd.edu/covid19.php>). AutoDock Vina<sup>17,18</sup> settings were applied as follows: energy\_range = 30, exhaustiveness = 80, num\_modes = 100, a combination which gave 20 binding modes per docking study. To thoroughly sample binding sites and modes on the spike surface, we conducted 20 runs of each docking procedure. A “docking procedure” being defined as one GAG model (HEP dimer or tetramer) docked into one spike receptor structure (e.g., a “docking procedure” could be described as dimeric HEP docked to WT spike in 1up state, clustered frame #1). Thus, with 20 replicas per docking procedure and 20 resultant binding modes per procedure, we obtained 400 binding modes per docking procedure. With 72 total docking procedures (2 GAG models, 3 spike variants, 2 spike conformational states, 6 receptor structures per spike variant/conformational state), we obtained 28,800 total binding modes from ensemble-based docking in this work.

We then used Scikit-learn's KMeans<sup>21</sup> clustering algorithm to cluster the geometric centers of all 28,800 resultant binding modes, and kneed, an inflection point calculation algorithm, to find the optimal number of clusters. From this clustering, we identified 19 distinctive GAG hotspots (**Figure S8**). To determine which of these 19 sites were accessible to long-chain HEP or HS, as would be encountered on the cell surface, we scanned all selected receptor structures (3 spike variants x 2 spike conformational states x 6 selected frames per variant/conformational state) to identify all residues within 10 Å of each hotspot centroid (for a full list of residues per site **Table S3**). As done in previous work,<sup>22</sup> we then used the Shrake-Rupley algorithm<sup>23</sup> to calculate the Accessible Surface Area (ASA) of each of these sites from the ~2  $\mu$ s of freely available MD trajectories provided by Casalino et al.<sup>7</sup> We used these simulations to estimate ASA of defined sites, as opposed to our own 50ns trajectories, because Casalino et al.'s are much longer, and

therefore likely to be more representative of conformational variability, especially with respect to glycan degrees of freedom. We calculated ASA for all sites at probe radii ranging from  $r=1.4 \text{ \AA}$  (reflective of water molecule probe),  $7.2 \text{ \AA}$  (reflective of small molecule binding or an antibody hypervariable loop), and  $18.6 \text{ \AA}$  (reflective of a small protein binding partner or antibody's variable fragment domain). We compared ASA results calculated at  $r=7.2 \text{ \AA}$  between all sites and saw that in the closed state (**Figure S9**), sites K, M, N, and R, were highly buried and likely not accessible to ligand binding. However, from the 1up state, site M becomes moderately exposed. Upon visualizing these sites on the spike structure with VMD we determined sites K, M, N, and R were indeed buried sites, however further investigation will be necessary to determine if site M does indeed become sufficiently exposed after spikes move into the 1up conformation. We then conducted further statistical analyses of these sites with MDAnalysis<sup>19,20</sup> as are described in the Supporting Information Results and Discussion below.

### 2.1.3 Schrödinger IFD:

In past work,<sup>22</sup> through ensemble-based docking, we identified 3 sites on the spike surface with high affinity to GAGs which could be important for anchoring the spike to long-chain GAG binding modes within the glycocalyx: the RBD cleft, the RBD patch, and the FCS. Ensemble-based docking studies in this current work (described above) reconfirmed the presence of these sites. Additionally, Brownian Dynamics simulations show the importance of the RBM as a potentially adapting kinetic discriminator for HS within the glycocalyx. While we have already incorporated a degree of protein and glycan motion with our ensemble-based docking studies -- by selecting clustered spike structures from 50ns of MD simulation -- local binding site conformations can adapt to ligand binding. To assess the degree to which local rearrangements at key binding sites could contribute to GAG binding and to see how these rearrangements do or don't change with the introduction of spike mutations, we conducted site specific flexible ligand-flexible receptor docking simulations with Schrödinger IFD (**Scheme S2**).<sup>24</sup> For docking into the RBD Cleft, RBD Patch, and FCS sites, the final frame from 50ns simulations of each variant closed spike structure was taken. Since the spike is a trimeric protein, there exist three RBD Cleft, RBD Patch, and FCS sites on the spike structure. To avoid complications and confounding variability due to glycan positioning during flexible docking simulations, we specifically then selected the specific RBD Cleft, RBD Patch, and FCS sites for docking based on which sites were not occupied by glycans in the final frame. This selection was particularly important as Schrödinger IFD does not handle or treat glycan atoms and therefore would not have been able to appropriately include glycan atoms during these studies. For docking into the RBM, we selected the final frame of 50 ns simulations of each variant 1up spike structure. No special care was needed for selecting frames without glycans in the case of the RBM as the RBM, when in the up/open state, is practically unreachable by spike glycans.

To prepare all spike structures for docking with Schrödinger IFD,<sup>24</sup> all protein structures were first titrated to pH 7.4 with PROPKA3.<sup>9</sup> Then all glycan atoms were removed from protein structures as Schrödinger does not properly treat glycans. HSD, HSE, and HSP residue names were converted to the Schrödinger compatible names HID, HIE, and HIP. Structures were then converted to .mae format and prepared according to OPLS4<sup>25</sup> force field using Schrödinger Protein Preparation Wizard<sup>10</sup> according to the following settings: missing hydrogen atoms were added (necessary after glycan deletion), bond orders were assigned, disulfide bonds were added (necessary as Schrödinger cannot also take topology files), hydrogen bonds were optimized with PROPKA3<sup>9</sup> at pH 7.4, and a restrained minimization of hydrogen atoms was

performed according to energies and forces described by the OPLS4<sup>25</sup> force field (again necessary after glycan deletion and addition of missing hydrogen atoms). All prepared protein structures will be shared with this work. Heparin and heparan sulfate tetrameric structures (specific chemical structures of which are shown in **Figure S19** below) were prepared for flexible docking with Schrödinger's LigPrep.<sup>26</sup>

Binding sites for flexible docking were then defined as the center of mass of the following residues, again with care taken to ensure no site was occupied by a glycan in the selected frame from MD simulations:

- **WT:**
  - **RBD Cleft:** (chain B and resid 346 348 349 351 352 354 355 356 357 450 454 466 467 469 489 472 490) or (chain C and resid 113 114 115 132 165 167)
  - **RBD Patch:** (chain B and resid 337 356 357 359 360 393 394 516 520 521 523 561 562 577 579 580 582) or (chain C and resid 41 170 172 173 226 227 228)
  - **FCS:** (chain B 675 676 677 678 679 680 681 682 683 684 685)
  - **RBM:** (chain A and resid 438 to 508)
- **Delta:**
  - **RBD Cleft:** (chain A and resid 346 348 349 351 352 354 355 356 357 450 454 466 467 469 489 472 490) or (chain B and resid 113 114 115 132 165 167)
  - **RBD Patch:** (chain B and resid 337 356 357 359 360 393 394 516 520 521 523 561 562 577 579 580 582) or (chain C and resid 41 170 172 173 226 227 228)
  - **FCS:** (chain B 675 676 677 678 679 680 681 682 683 684 685)
  - **RBM:** (chain A and resid 438 to 508)
- **Omicron:**
  - **RBD Cleft:** (chain A and resid 346 348 349 351 352 354 355 356 357 450 454 466 467 469 489 472 490) or (chain B and resid 113 114 115 132 165 167)
  - **RBD Patch:** (chain B and resid 337 356 357 359 360 393 394 516 520 521 523 561 562 577 579 580 582) or (chain C and resid 41 170 172 173 226 227 228)
  - **FCS:** (chain B 675 676 677 678 679 680 681 682 683 684 685)
  - **RBM:** (chain A and resid 438 to 508)

From each docking procedure, Glide scores were collected and analyzed holistically as well as individual binding modes were inspected to determine interactions of interest within each binding site.

#### **2.1.4 Brownian Dynamics Simulations:**

Following the preparation and docking of glycoproteins and ligands, all structures were submitted to the PDB2PQR program<sup>27,28</sup> to assign atomic partial charges and radii according to the CHARMM36m forcefield.<sup>14-16</sup> Protonation states for all systems were assigned using PROPKA3<sup>9</sup> at pH of 7.4. Then the “make\_apbs\_input” and “run\_apbs\_input” programs in the Browndye2 package<sup>29,30</sup> were used to prepare input files and run APBS 1.5<sup>31-36</sup> to solve the linear Poisson-Boltzmann equation for the creation of electrostatic potential grids for each molecule. Electrostatics calculations, as well as BD simulations, were performed at a temperature of 298.15K, with a NaCl electrolyte concentration of 10mM, a solvent dielectric of 78, and a solute interior dielectric of 4, and with a grid spacing of 0.5Å.



BD simulations to study the association kinetics of bimolecular reactions require definitions of reaction criteria. Following the docking procedure, key interacting residues for each of the sites on the glycoproteins were identified. For each site on each monomer of each glycoprotein, the center of mass of these residues was computed. Separately, the center of mass for each ligand was also computed. The distance between the glycoprotein site center of mass and the ligand center of mass was used as the reaction coordinate, and if this distance ever fell below a defined threshold of 14Å, a “reaction” was assumed to have occurred.

The Browndye2 package<sup>29,30</sup> as used to prepare and run all BD simulations. Hydrodynamics were enabled. Upon independent investigation, we observed anomalous behavior for these systems when desolvation forces were enabled, most likely due to the high magnitude of molecular charges involved. For this reason, we chose not to enable desolvation forces for these simulations. A total of 24 separate systems were simulated on the TACC Frontera supercomputer. For each system, the BD simulations were spread onto a 56-core node and ran for 24 hours. The total number of BD simulations varied between systems, and anywhere from a few hundred to a hundred thousand separate trajectories were completed per system. Following the simulations, the obtained reaction statistics may be used to estimate  $k_{onS}$  for each system. BD simulations were performed on TACC Frontera.

To compute the association rate constants to the b-surface, we use the following equation, which is derived from the Smoluchowski equation:<sup>37,38</sup>

$$k(r) = - \frac{DQ_cQ_s}{\left[1 - \exp\left\{\frac{Q_cQ_s}{4\pi\epsilon_0\epsilon_r k_B T r}\right\}\right] \epsilon_0\epsilon_r k_B T}$$

Where  $k(r)$  is the association rate constant to the spherical b-surface of radius  $r$ ,  $Q_s$  is the charge of the substrate,  $Q_c$  is the charge of the receptor,  $D$  is the radial relative diffusion coefficient of the two molecules,  $\epsilon_0$  is the vacuum permittivity,  $\epsilon_r$  is the dielectric constant of the solvent,  $k_B$  is the Boltzmann constant, and  $T$  is the system temperature.

### 2.1.5 Spike RBD+ACE2 MD Simulations:

To investigate the stability of the ACE2/RBD interface over the course of the variant timeline, RBD+ACE2 systems were constructed for WT, Delta, and Omicron variants. RBDs were extracted from our full spike WT, Delta, and Omicron models and then aligned to a 2.90 Å cryo-EM structure of the WT ACE2/RBD complex (PDB ID 6M17).<sup>39</sup> ACE2 and aligned RBD complex were extracted for each variant and full glycosylation profile of ACE2 and RBD were replicated from Barros et al.<sup>40</sup> PROPKA3<sup>9</sup> was used to ensure all protonation states for ACE2 and the RBDs were still appropriate, and they were. Special attention was paid to ensure the Zn<sup>2+</sup> atoms from ACE2 were retained in RBD/ACE2 system model building. Additionally, special care was taken to make sure there were no residue clashes along the RBD/ACE2 interface as the Delta and Omicron interfaces were constructed from alignment to the WT RBD structure and not resolved experimentally. All systems were solvated in water boxes of ~130 x 140 x 180 Å<sup>3</sup> and ionized with 0.15M NaCl. For each RBD/ACE2 system, we then performed 3 replicas of the following MD simulation protocol with NAMD2.14<sup>12,13</sup> and CHARMM36m all atom force field:<sup>14-16</sup> 10,000 steps of Steepest Descent minimization for all atoms (no restraints nor constraints). Heating of the solvated system from 10K to

310K by increments of 25K with protein and glycan atoms held in light restraint according to a force constant of 1 kcal/mol/Å. With each increase in temperature, 10080 steps (1fs/step) of MD simulation were performed within the NVT ensemble. Once the temperature reached 310K, 0.5 ns of NVT equilibration was performed with restraints maintained. NpT equilibration (310K, 1.01325 bar) for 0.5 ns (1fs/step) with restraint (force constant = 1 kcal/mol/Å) applied to all protein backbone atoms. Pressure was maintained a Langevin barostat. Box cell dimensions were set to flexible during pressure equilibration. GPU accelerated NVT free (no restraints) production (310K, 1.01325 bar) simulations for 25 ns (1fs/step) conducted with NAMD3.0.<sup>13</sup> As system pressure was equilibrated in the prior step, box cell flexibility was turned off in this step (useFlexibleCell = no). GPU accelerated NVT production runs were performed on the Hopper GPU cluster at SDSC TSCC. To prepare for analysis, VMD<sup>11</sup> was used to align trajectories according to protein C<sub>α</sub> atomic positions in the first frame, and water and ion atoms were stripped from trajectories. Trajectories were then ported into MDAnalysis<sup>19,20</sup> as universes where native contacts analysis was performed.

### 2.1.6 Dynamical Electrostatic Potential Map Calculations:

To confirm the presence of large, positively charged regions on the spike surface we used a time-averaged implementation of Adaptive Poisson Boltzmann Solver (APBS)<sup>31-36</sup> to calculate the electrostatic potential at equally spaced grid points along the spike surface over our aligned 50ns classical MD simulation trajectories (described in **Section 2.1.1** above). We calculated electrostatic potential maps for the WT spike in closed and open states as well as for Delta and Omicron BA.1 variants full-length spike structures in the closed and open states. All resulting ESP volume (.dx) files for each frame of the 50ns trajectories (1260 frames per simulation) were averaged using the APBS's dxmath functionality. For each structure and each frame, we calculated electrostatic potential maps using the following options, and example input scripts can be found in the downloadable tar.gz file associated with this supporting information:

```
elec name frame
      mg-auto
      dime 321 321 321
      cglen 400 400 400
      fglen 200 200 200
      cgcent mol 1
      fgcent mol 1
      lpbe
      bcf1 sdh
      ion charge 1 conc 0.150 radius 1.36375
      ion charge -1 conc 0.150 radius 2.27
      pdie 4.0
      sdie 78.00
```

```
chgm spl2
srfm smol
srad 1.4
swin 0.3
sdens 10.0
temp 298.15
gamma 0.105
calcenergy total
write pot dx frame
end
```

## **2.2 Experimental Methods:**

### **2.2.1 Materials**

Heparin (HEP001) was purchased from Galen laboratory supplies. Heparan sulfate from bovine kidney (H7640), Human serum albumin (A3782), and sucrose (S0389), Silver lactate (359750), Hydroquinone (H9003) were purchased from Sigma-Aldrich. Biotin-PEG3-amine (BG-17) was purchased from G-Biosciences. Tween 20 (J20605-AP) was purchased from Thermo Fisher Scientific. Sodium phosphate monobasic (389872500) and Sodium phosphate dibasic (204851000) were purchased from ACROS Organics. Bovine serum albumin (105033) was purchased from MP biomedical. Gold nanoparticles 10nm (15703-20) were purchased from Ted Pella Inc. Human ACE2, Fc Tag (AC2-H5257) was purchased from Acro Biosystems. Rabbit anti-human IgG (31143) and Horseradish peroxidase conjugated goat anti-human IgG with Horseradish peroxidase (A18811) was purchased from Invitrogen. Horseradish peroxidase conjugated anti-His Tag antibody (652504) was purchased from Biolegend. Nitrocellulose membrane (FF120HP), sample pad (Whatman CF4 dipstick pad), and absorbent pad (Whatman standard 17) were purchased from Cytiva. SARS-CoV-2 Wild type Spike (40589-V08H4), Delta (40589-V08H10) Spike, and Omicron (40589-V08H26) Spike, and HIV gp140 envelope protein (11677-V08H) were purchased from Sino biological. SARS-CoV-2 Alpha (B.1.1.7) Spike (10796-CV-100) and Beta (B.1.351) spike (10786-CV-100) were purchased from R&D systems. Streptavidin modified BLI biosensor tips (18-5019) and anti-human IgG Fc Capture (AHC) BLI biosensor tips (18-5060) were purchased from Sartorius. N-Terminal domain binding antibody (LT-2000) was purchased from Leinco Technologies. Human saliva pooled from human donors (991-05-P) was purchased from LEE Biosolutions.

### **2.2.2 Biotin conjugation to heparin**

For BLI, ELISA, and LFSA preparation, biotin modified heparin was prepared. Specifically, 2 mg of biotin-PEG3-amine and 2 mg of heparin was dissolved in the 10 mM sodium phosphate buffer pH 7.4. Followed by the addition of the sodium cyanoborohydride (5 mg), and the solution was incubated 24 hr at 60°C. After the incubation, same amount of sodium cyanoborohydride was added and incubated for another 24

hr. Resulting solution was purified by centrifugation with 3k filter to remove the unreacted biotins. Finally, the solution was lyophilized and stored in -20°C until further use.

### **2.2.3 Immobilization and binding of heparin, ACE2 to variant spike proteins**

To compare the binding of heparin or ACE2 to variant spike proteins, enzyme-linked immunoassay (ELISA) was utilized. Firstly, streptavidin (200 nM; 50 µL) was added to the Nunc maxisorp flat bottom 96 well plate and incubated overnight at 4°C. The plates were washed with 200 µl of 1xPBST (0.05% tween-20) three times to remove unbound streptavidin. Then the plate was blocked with 100 µl of 2% BSA for 1 hr at room temperature and washed with 1xPBST. Biotinylated heparin (800 nM; 50 µL) was incubated for 1hr and washed thoroughly to remove unbound heparin. SARS-CoV-2 Spike proteins (WT, Alpha, Beta, Delta, and Omicron; 100 nM; 50 µL) in LFS buffer were incubated for 1 hr, and LFS buffer without any spike protein was also incubated for 1 hr as a control. After 1 hr incubation, wells were washed with 200 µl of 1xPBST three times. For the signal generation, anti-his tag-HRP (1 µg/ml; 50 µl) was incubated for 30 min. To remove the unbound HRP, plates were thoroughly washed 5 times with 1xPBST. Finally, 50 µl of TMB substrate (Thermo Fisher Scientific, 34028) was added to each well to develop color. The reaction was stopped by adding 50 µl of stop solution (Thermo Fisher Scientific, N600), and absorbance was measured at 450 nm. In case of ACE2 binding, same procedure was used as heparin binding except that ACE2 functionalized plates were prepared by directly absorbing ACE2 (10 µg/mL; 50 µL) to Nunc maxisorp flat bottom 96 well plates at 4 °C overnight instead of streptavidin functionalization.

### **2.2.4 Biolayer interferometry (BLI)**

For measuring the binding affinities of heparin or ACE2 to variants of SARS-CoV-2 Spike, biolayer interferometry (BLI) was used. For heparin binding affinity measurement, streptavidin coated BLI tips were functionalized with biotin-heparin (100 µg/mL, 40 µL) for 180 s. Unbound or loosely bound biotin-heparin was washed for 500 s. Heparin functionalized tips were treated with various concentrations of spike protein (10, 25, 50, 100, 200 nM) including control without spike protein for 400 sec and dissociation was measured for 500 s. Binding affinity, Dissociation Constant ( $K_D$ ), was calculated with steady-state analysis using the HT 11.1 software. ACE2 binding affinity was measured with the same procedure except that anti-human IgG Fc capture (AHC) BLI tips were utilized when ACE2 (1 µg/mL; 40 µL) was loaded. For all measurements, LFS buffer (10 mM Sodium phosphate, 0.05% tween-20, pH 7.4) was used.

### **2.2.5 Checking ternary complex formation (Spike-HS-ACE2) using ELISA**

To check the synergy of heparin and ACE2 binding in spike protein binding, ELISA was utilized. Firstly, streptavidin (200 nM; 50 µL) was added to the Nunc maxisorp flat bottom 96 well plate and incubated overnight at 4°C. The plates were washed with 1xPBST (0.05% tween-20) three times to remove unbound streptavidin. Then the plate was blocked with 2% BSA (100 µl) for 1hr at room temperature and washed with 1xPBST. Biotinylated heparin (800 nM; 50 µL) was incubated for 1hr and washed thoroughly to remove unbound heparin. SARS-CoV-2 Spike proteins (100 nM; 50 µL) in LFS buffer were incubated for 1 hr including the control without spike proteins. After incubation wells were washed three times with

1xPBST to remove unbound spike proteins. ACE2 (1 ug/mL; 50  $\mu$ L) in LFS buffer was added and incubated for 1 hr. After incubation, each well was washed three times with 1xPBST. Finally, anti-IgG-HRP (1  $\mu$ g/mL; 50  $\mu$ L) was incubated for 30 min, and plates were thoroughly washed 5 times with 1xPBST. Finally, 50  $\mu$ L of TMB substrate (Thermo Fisher Scientific, 34028) was added to each well to develop color. The reaction was stopped by adding 50  $\mu$ L of stop solution (Thermo Fisher Scientific, N600), and absorbance was measured at 450 nm.

### **2.2.6 Checking ternary complex formation (Spike-HS-ACE2) using Mass Photometer**

To measure the synergy effect of heparan sulfate and ACE2 in spike protein binding, mass photometry (Refeyn One mass photometry) was utilized. Using heparin on mass photometer drastically reduced number of spike protein counts even though the same concentration of omicron spike trimer and glycans were used (**Figure S20**). This is likely due to the fact that the high number of negative charges on heparin might hinder the contacting of spike protein to the surface of the glass, resulting in a low number of count event. Therefore, heparan sulfate instead of heparin was utilized to check the ternary complex formation on mass photometer. Microscope coverslips (CG15KH1, 24 x 50 mm, Thickness  $170 \pm 5$   $\mu$ m, Thorlabs) were cleaned by sonication in 2-Propanol (A516-4, Fisher Scientific) followed by DW (10 min for each step). Silicone gasket (3 mm diameter x 1mm depth, Grace Bio-labs) was applied to the cleaned coverslip to form a chamber. After preparing the gasket, 10  $\mu$ L of LFS buffer (10 mM sodium phosphate, pH 7.4) without tween-20 was first injected to the chamber to find the focus using the autofocus function called droplet-dilution using Acquire MP Software provided by the instrument. Samples (Spike, Spike + ACE2, Spike + HS + ACE2) were prepared by incubating Spike (40  $\mu$ g/ml; 5  $\mu$ L), ACE2 (16  $\mu$ g/ml; 2.5  $\mu$ L), and HS (2  $\mu$ g/ml; 2.5  $\mu$ L) for 30 min at room temperature prior to mass photometer. For each acquisition, 10  $\mu$ L of mixture of protein solution was introduced to the chamber (total volume: 20  $\mu$ L) and movies of 60 s duration were recorded. Each sample was measured in new chambers (each chamber was used once). All mass photometer data were analyzed with DiscoverMP (2022 ver. R1). Firstly, using a mass calibration curve, ratiometric data was converted to the mass. Then, to check the fraction of the ternary complexes, count numbers for binding event were obtained for each mass range (denoted as group A, B, and C). Obtained count numbers were used to calculate the relative fraction of each and compare the fraction of the ternary complex with or without HS.

### **2.2.7 Preparation of signaling probes**

To prepare the signaling probes, ACE2 and NTD Ab were conjugated to the gold nanoparticles (AuNP). Firstly, 10 nm AuNP (1 ml) was equilibrated with borate buffer (0.1 M pH 8.0; 100  $\mu$ L), then ACE2 (0.6 mg/ml; 8.3  $\mu$ L) or NTD Ab (1 mg/ml; 5  $\mu$ L) was added to prepare the signaling probes for *GlycoGrip2.0* and *GlycoGrip1.0*, respectively. After incubating the resulting solution for 1 hr at room temperature with continuous rotation, 100  $\mu$ L of 1% BSA was added and incubated for an additional 30 min. To remove the unbound proteins, ACE2 or NTD Ab conjugated AuNPs were centrifugated at 22000g, 4°C for 45 min and the supernatant was removed. AuNP pellets were resuspended in the 1% BSA (1 ml) solution. This procedure was repeated 3 times. Finally, ACE2 or NTD Ab conjugated AuNPs were resuspended in the LFS buffer and stored in 4°C until further use.

### **2.2.8 Preparation of *GlycoGrip* LFSA**

For the immobilization of the heparin to the nitrocellulose membrane, heparin was conjugated to the streptavidin as previously reported. Briefly, biotin-heparin (2 mg/ml, 50  $\mu$ l) was incubated with streptavidin (1 mg/ml, 100  $\mu$ l) for 1 hr. The mixture solutions were purified by centrifugation with a 30k amicon filter to remove excess biotin-heparin. The concentration of heparin was measured using Azure A assay. Heparin conjugated with streptavidin (300  $\mu$ M) and rabbit antihuman IgG (1 mg/mL) were dispensed on the nitrocellulose membrane (FF120HP). Dispensed nitrocellulose membrane was dried at 65 °C for 3 min. After drying, the nitrocellulose membrane was blocked with a blocking buffer (1% BSA, 0.05% Tween 20 in 10 mM PB, pH 7.4). Finally, the sample pad (Whatman CF4 dipstick pad) and the absorbent pad (Whatman standard 17) were assembled onto the nitrocellulose membrane. Assembled strips were stored at room temperature with desiccant before use.

### **2.2.9 Comparison of the variant detection in *GlycoGrip1.0* and *GlycoGrip2.0***

For the comparison of the SARS-CoV-2 variant detection in *GlycoGrip1.0* and *GlycoGrip2.0*, 25  $\mu$ L of each of the Spike proteins (25  $\mu$ g/ml) in LFSA buffer were incubated with 25  $\mu$ l of signaling probes (i.e., 20 nM of NTD Ab-AuNP for *GlycoGrip1.0*, and 20 nM of ACE2-AuNP for *GlycoGrip2.0*) for 30 min at room temperature. Then, the dipstick method was used to compare the detection. Briefly, the resulting solutions were dispensed in the flat bottom 96 well plate and lateral flow strips were dipped for 10 min. After 10 min, the image was taken by smartphone camera and signals were quantitatively analyzed by ImageJ software.

### **2.2.10 Evaluation of Selectivity and sensitivity of *GlycoGrip2.0***

To evaluate the selectivity of the *GlycoGrip2.0*, 25  $\mu$ L of each samples including SARS-CoV-2 Omicron spike (25  $\mu$ g/mL), CoV1 S1 (25  $\mu$ g/mL), MERS S1 (25  $\mu$ g/mL), HIV gp140 (group M, CRF07\_BC) envelope protein (25  $\mu$ g/mL), Human serum albumin (50 mg/mL), and Human saliva (25x diluted from the stock solution) was incubated with 25  $\mu$ L of signaling probe (ACE2-AuNP; 20 nM) for 30 min. Then, signals were generated with the dipstick method and analyzed with ImageJ.

For the sensitivity testing, different concentrations of SARS-CoV-2 Omicron spike (0, 0.4, 0.8, 1.6, 3.13, 6.25, 12.5, 25, 50  $\mu$ g/ml; 25  $\mu$ l) were incubated with ACE2-AuNP (20 nM; 25  $\mu$ l) for 30 min. After 30 min, the same dipstick method was utilized. Signal intensity of the test line was analyzed with ImageJ software and the limit of the detection (LOD) was estimated by blank + 3 standard deviations. At least 3 independent tests were performed to calculate the LOD.

### **2.2.11 Evaluation of sensitivity of *GlycoGrip2.0* in human saliva**

For human saliva testing, various concentrations of SARS-CoV-2 Omicron spike (0, 0.8, 1.6, 6.25, 25, 50, 100  $\mu$ g/ml; 12.5  $\mu$ l) were introduced into human saliva (25 $\mu$ L; 25x diluted from the stock solution). Prepared spike in human saliva solution were incubated with ACE2-AuNP (20 nM; 25  $\mu$ L) for 30 min. After

30 min, dipstick method was utilized, and signal was enhanced with silver enhancement methods as described in 2.2.12.

### 2.2.12 Signal enhancement analysis

To enhance the sensitivity of the *GlycoGrip2.0*, silver enhancement methods<sup>41</sup> was adopted. Specifically, different concentrations of SARS-CoV-2 Omicron spike (0, 0.1, 0.2, 0.4, 0.8, 1.6, 3.13, 6.25, 12.5, 25, 50 ug/mL; 25  $\mu$ L) were incubated with ACE2-AuNP (20 nM; 25  $\mu$ L) for 30 min. After 30 min, each solution was dispensed to 96 well plates and LFSA strips were dipped for 10 min. After 10 min, Strips were sequentially washed with LFSA buffer (100  $\mu$ L) and DW (100  $\mu$ L) for 3 min. Finally, Strips were dipped into the mixture of 0.3% silver lactate and 3% hydroquinone (100  $\mu$ L each) for 3 min and the enhancement reaction was stopped by washing with DW. Signal intensity of the test line was analyzed with ImageJ software and the limit of the detection (LOD) was estimated by blank + 3 standard deviations. At least 3 independent tests were performed to calculate the LOD.

## 2.3 Supplemental notes:

### 2.3.1 Summary of AutoDock Vina results:

28,800 GAG binding modes were collected from ensemble-based docking studies as laid out in Scheme S1 below. All binding modes for WT, Delta, and Omicron spike structures in closed and 1up conformations can be seen in **Figures S4, S5, and S6** respectively. The centers of mass of each of these resultant binding modes were collected passed through kmeans clustering to identify GAG binding “hotspots” on the spike surface. Figure S7 shows the sum of squared Euclidean distances (SSE) for the generated 1-100 clusters; kneed elbow locator algorithm was used to determine 19 to be the optimal number of clusters of all 28,800 binding modes. These 19 clusters were then given names A-S and their locations on the spike structure were identified, **Figure S8**. To determine which of these binding sites were “surface exposed”, i.e. sites accessible to long chain GAGs within the glycoalyx, we calculated the Accessible Surface Area (ASA) for each of these sites using the Shrake-Rupley algorithm<sup>19</sup> through VMD tools,<sup>11</sup> **Figure S9**, with a probe radius of  $r=7.2$  Å from WT trajectories shared for closed and 1up state spike proteins shared by Casalino et al.<sup>8</sup> Each site was defined as any residue (from all structures considered, i.e., all conformations of WT, Delta, and Omicron structures) within 10 Å of the centroid of said site as defined by kmeans clustering. A probe radius of 7.2 Å was chosen to be consistent with an approaching GAG fragment. All residue numbers per site can be found in **Table S3**. From ASA results we see that in the closed spike conformation, sites K, M, N, and R are largely inaccessible to GAG fragments within the glycoalyx. However, in the 1up spike conformation site M becomes marginally exposed due to the lifting up of the neighboring RBD.

To identify any sites of particular importance on a per spike variant basis we then analyzed the distributions of predicted binding energies within each site as given by AutoDock Vina,<sup>17,18</sup> **Figure S10**. As can be seen from these results, both heparin dimers and heparin tetramers bind with relatively similar predicted energies to all sites on a per variant basis, save for a few instances. We also compared the distribution of predicted binding energies at each site as a function of spike conformation, i.e., closed versus 1up states, **Figure S11**. Again, very little difference could be seen between closed and 1up spike

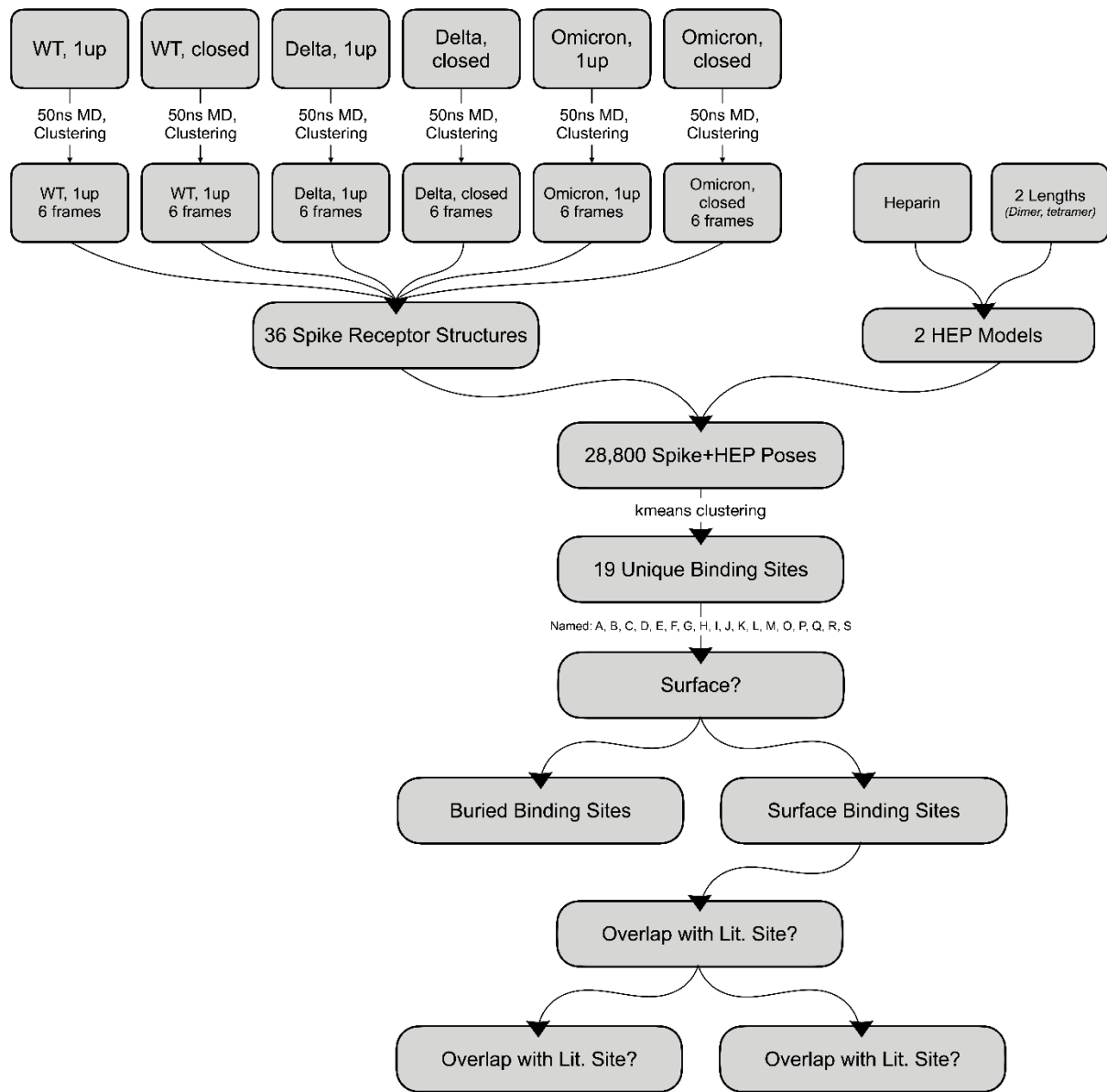
structures to suggest heparin dimers or tetramers favor binding to either state. Given the similarity in predicted energies, and the broad distribution of predicted energies at each site in all resultant binding modes, we cannot predict, at this time, any significant differences in binding affinity at each site resulting from changes in spike sequence. As such we predict binding affinity differences as observed with BLI between heparin and variant spike structures are likely due to effects only captured by use of long-chain heparins or due to kinetic effects such as rate of encounter complex formation.

### 2.3.2 Summary of Schrödinger IFD Results:

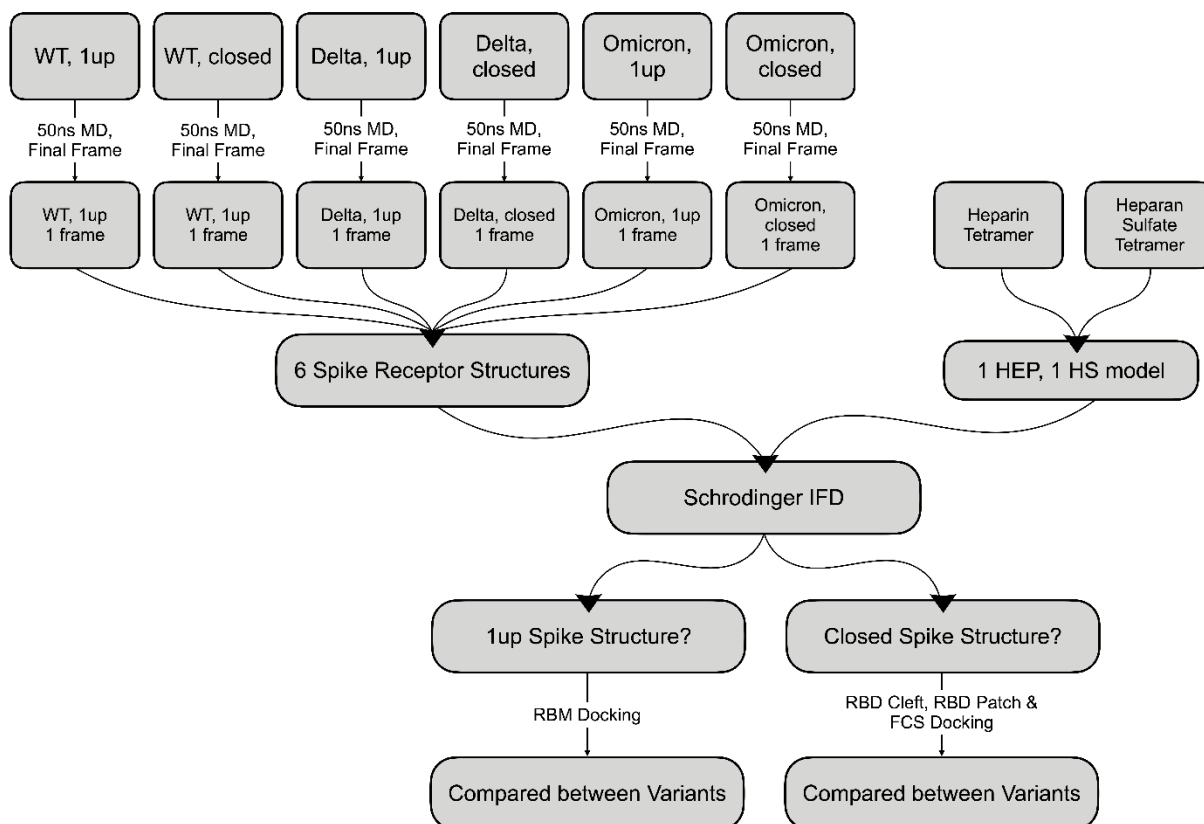
While we have already incorporated a degree of protein flexibility in our docking studies by conducting extensive ensemble-based sampling (i.e., 3 spike proteins (WT, Delta, Omicron) x 2 spike states (closed, 1up) x 6 conformations each = 36 total spike receptor structures) we were interested in identifying any potential induced fit effects and how such effects may adapt/change over the variant timeline. As such we conducted flexible ligand-flexible receptor docking studies with Schrödinger IFD on targeted sites within the spike protein using heparin and heparan sulfate tetrameric models. From these results, **Figure S12**, we again see predicted binding energies (Glide Scores) are broad at each site, and there is virtually no difference in these distributions across the variant timeline despite mutations within each site. We predict that this is due to the innate flexibility of GAG molecules like heparin and heparan sulfate. These ligands can adapt to mutations within these binding sites and thus still bind at each site. Thus, we predict differences in binding affinity between heparin/heparan sulfate and spike proteins as seen from BLI and ELISA results are likely due to effects that can only be seen at the long-chain binding mode scale or due to kinetic effects not captured in docking studies.

Schemes:





**Scheme S1:** Schematic outlining variant spike simulation, clustering, and AutoDock Vina procedures as discussed in Computational Methods Sections 2.1.1 to 2.1.2.



**Scheme S2:** Schrödinger IFD Methodology at pH 7.4 outlining variant spike simulation, clustering, and Schrödinger IFD procedures as discussed in Computational Methods 2.1.1 and 2.1.3.

### Tables:

**Table S1:** Complete list of all mutations per variant considered for modeling and charge calculations in this work. Glycan contribution calculated according to Watanabe et al.<sup>6</sup> and with glycans chosen consistent to Casalino et al.<sup>8</sup> with 14 sialic acid residues included (total glycan charge of  $-14$ ).

| Variant | Mutations from WT/2019 (charge change relative to WT due to mutation)   | $\Delta T_Q$   | $T_Q$ |
|---------|---|----------------|-------|
| WT      |   |                | -11   |
| Alpha   | $\Delta H69-V70$ (0), $\Delta Y144$ (0), A570D (-1), D614G (+1), P681H (0), T716I (0), S982A (0), D1118H (+1) | $(+1)*3 = +3$  | -8    |
| Beta    | D80A (+1), D215G (+1), $\Delta L241-L242-A243$ (0), K417N (-1), E484K (+2), N501Y (0), D614G (+1), A701V (0)  | $(+4)*3 = +12$ | +1    |

|                |  |              |     |
|----------------|--|--------------|-----|
| Delta          | T19R (+1), G142D (-1), ΔE156-F157 (+1), R158G (-1), L452R (+1), T478K (+1), D614G (+1), P681R (+1), D950N (+1), ΔN17-Glycan (0)  | (+5)*3 = +15 | +4  |
| Omicron (BA.1) | A67V (0), ΔH69-V70 (0), T95I (0), G142D (-1), ΔV143-Y144-Y145 (0), ΔN211 (0), L212I, ins214EPE (-2), G338D (-1), S371L (0), S373P (0), S375F (0), K417N (-1), N440K (+1), G446S (0), S466N (0), T478K (+1), E484A (+1), Q493R (+1), G498R (+1), N501Y (0), Y505H (0), T547K (+1), D614G (+1), H655Y (0), N679K (+1), P681H (0), N764K (+1), D796Y (+1), N856K (+1), Q954H (0), N969K (+1), L981F (0) | (+7)*3 = +21 | +10 |

**Table S2:** Complete list of all titratable residues and their selected protonation states each spike/ACE2 structure to pH = 7.4, as calculated by PROPKA. Full pK<sub>a</sub> calculation data can be found in the shared files associated with this supporting information.

| pH  | Prot | Cnf  | P.S. | Residue IDs   |
|-----|------|------|------|---|
| 7.4 | WT   | Clo. | ASP  | 40 53 80 88 111 138 178 198 215 228 253 287 290 294 364 389 398 405<br>420 427 428 442 467 568 571 574 578 586 614 627 663 767 745 775<br>796 808 820 830 839 843 848 867 936 950 979 985 994 1041 1084 1118<br>1127 1139 |
|     |      |      | ASPP | none  |
|     |      |      | GLU  | 96 132 154 156 169 180 191 224 281 598 309 324 340 406 465 471 484<br>516 554 583 619 654 661 702 725 748 773 780 819 868 918 988 990<br>1017 1031 1072 1092 1111   |
|     |      |      | GLUP | none  |
|     |      |      | HSD  | 146 207 245 519 1058  |
|     |      |      | HSE  | 49 66 69 625 655 1048 1064 1083 1101  |
|     |      |      | HSP  | none  |
| 7.4 | WT   | 1up  | ASP  | 40 53 80 88 111 138 178 198 215 228 253 287 290 294 364 389 398 405<br>420 427 428 442 467 568 571 574 578 586 614 627 663 767 745 775<br>796 808 820 830 839 843 848 867 936 950 979 985 994 1041 1084 1118<br>1127 1139 |
|     |      |      | ASPP | none  |
|     |      |      | GLU  | 96 132 154 156 169 180 191 224 281 598 309 324 340 406 465 471 484<br>516 554 583 619 654 661 702 725 748 773 780 819 868 918 988 990<br>1017 1031 1072 1092 1111   |

|     |     |      |      |   |
|-----|-----|------|------|---|
|     |     |      | GLUP | none  |
|     |     |      | HSD  | 146 207 245 519 1058  |
|     |     |      | HSE  | 49 66 69 625 655 1048 1064 1083 1101  |
|     |     |      | HSP  | none  |
| 7.4 | Del | Clo. | ASP  | 40 53 80 88 111 138 142 178 198 215 228 253 287 290 294 364 389 398<br>405 420 427 428 442 467 568 571 574 578 586 627 663 737 745 775<br>796 808 820 830 839 843 848 867 936 979 985 994 1041 1084 1118<br>1127 1139     |
|     |     |      | ASPP | none  |
|     |     |      | GLU  | 96 132 154 169 180 191 224 281 298 309 324 340 406 465 471 484 516<br>554 583 619 654 661 702 725 748 773 780 819 868 918 988 990 1017<br>1031 1072 1092 1111   |
|     |     |      | GLUP | none  |
|     |     |      | HSD  | 519 625 655 1058 1083 1088  |
|     |     |      | HSE  | 49 66 69 146 207 245 1048 1064 1101   |
|     |     |      | HSP  | None  |
| 7.4 | Del | 1up  | ASP  | 40 53 80 88 111 138 142 178 198 215 228 253 287 290 294 364 389 398<br>405 420 427 428 442 467 568 571 574 578 586 627 663 737 745 775<br>796 808 820 830 839 843 848 867 936 979 985 994 1041 1084 1118<br>1127 1139     |
|     |     |      | ASPP | none  |
|     |     |      | GLU  | 96 132 154 169 180 191 224 281 298 309 324 340 406 465 471 484 516<br>554 583 619 654 661 702 725 748 773 780 819 868 918 988 990 1017<br>1031 1072 1092 1111   |
|     |     |      | GLUP | none  |
|     |     |      | HSD  | 519 625 655 1058 1083 1088  |
|     |     |      | HSE  | 49 66 69 146 207 245 1048 1064 1101   |
|     |     |      | HSP  | None  |
| 7.4 | Omi | Clo. | ASP  | 40 53 80 88 111 138 142 178 198 215 228 253 287 290 294 339 364 389<br>398 405 420 427 428 442 467 568 571 574 578 586 627 663 737 745<br>775 808 820 830 839 843 848 867 936 950 979 985 994 1041 1084 1118<br>1127 1139 |

|     |      |     |      |   |
|-----|------|-----|------|---|
|     |      |     | ASPP | none  |
|     |      |     | GLU  | 96 132 154 156 169 180 191 2141 (inserted E) 2143 (inserted E) 224 281<br>298 309 324 340 406 465 471 516 554 583 619 654 661 702 725 748<br>773 780 819 868 918 988 990 1017 1031 1072 1092 1111                         |
|     |      |     | GLUP | None  |
|     |      |     | HSD  | 146 207 245 519 681 1058 1088   |
|     |      |     | HSE  | 49 66 505 625 954 1048 1064 1083 1101   |
|     |      |     | HSP  | none  |
| 7.4 | Omi  | 1up | ASP  | 40 53 80 88 111 138 142 178 198 215 228 253 287 290 294 339 364 389<br>398 405 420 427 428 442 467 568 571 574 578 586 627 663 737 745<br>775 808 820 830 839 843 848 867 936 950 979 985 994 1041 1084 1118<br>1127 1139 |
|     |      |     | ASPP | none  |
|     |      |     | GLU  | 96 132 154 156 169 180 191 2141 (inserted E) 2143 (inserted E) 224 281<br>298 309 324 340 406 465 471 516 554 583 619 654 661 702 725 748<br>773 780 819 868 918 988 990 1017 1031 1072 1092 1111                         |
|     |      |     | GLUP | None  |
|     |      |     | HSD  | 146 207 245 519 681 1058 1088   |
|     |      |     | HSE  | 49 66 505 625 954 1048 1064 1083 1101   |
|     |      |     | HSP  | none  |
| 7.4 | ACE2 | --  | ASP  | 30 38 67 111 136 157 198 201 206 213 216 225 269 292 295 299 303<br>335 350 355 367 368 382 427 431 471 494 499 509 543 597 609 615<br>630 637 669 693 713 719  |
|     |      |     | ASPP | none  |
|     |      |     | GLU  | 22 23 35 37 56 57 75 87 110 140 145 150 160 166 171 181 182 189 197<br>208 224 227 231 232 238 310 312 329 375 398 402 406 430 433 435<br>457 467 479 483 489 495 527 536 549 564 571 589 634 639 667 668<br>699 701 723  |
|     |      |     | GLUP | none  |
|     |      |     | HSD  | 34 195 239 373 374 378 417 493  |
|     |      |     | HSE  | 228 241 265 345 401 505 535 540   |
|     |      |     | HSP  | none  |

Prot. = protein. Cnf = conformational state, relevant to spike protein structures only. P.S. = protonation state. Clo. = spike in closed conformational state. 1up = spike in 1up/open conformational state. WT = Wild Type. Del. = Delta. Omi. = Omicron. ACE2 = angiotensin converting enzyme 2. ASP = deprotonated/negatively charged aspartate. ASPP = protonated/neutral aspartate. GLU = deprotonated/negatively charged glutamate. GLUP = protonated/neutral glutamate. HSD = singly protonated/neutral histidine with protonation on the N<sub>δ</sub> atom. HSE = singly protonated/neutral histidine with protonation on the N<sub>ε</sub> atom. HSP = double protonated/positively charged histidine with protonation on N<sub>δ</sub> and N<sub>ε</sub> atoms.

**Table S3:** Complete list of protein residues per GAG binding hotspot as predicted by ensemble-based docking with AutoDock and Kmeans clustering.

| Site | Protein Residues: Residue Name, Residue Number, Chain ID<br><br>Glycans: Glycan Protein Residue Name, Protein Residue Number, (Protein Chain ID)   |
|------|--|
| A    | Arg403A, Asp405A, Glu406A, Asn417A, Lys417A, Tyr421A, Ser443A, Lys444A, Val445A, Gly446A, Asn448A, Tyr449A, Tyr451A, Leu452A, Tyr453A, Leu455A, Phe456A, Lys458A, Ser459A, Asn460A, Lys462A, Ser477A, Phe490A, Leu492A, Gln493A, Arg493A, Ser494A, Tyr495A, Ser496A, Phe497A, Gly496A, Gln498A, Arg498A, Pro499A, Thr500A, Asn501A, Tyr501A, Gly502A, Val503A, Gly504A, Tyr505A, His505A, Gln506A, Pro507A, Phe342B, Asn343B, Tyr369B, Asn370B, Leu371B, Ser371B, Ala372B, Ser373B, Pro373B, Ser375B, Phe375B, Phe374B, Trp436B, Asn437B, Ser438B, Asn439B, Asn440B, Lys440B, Leu441B, Gly447B, Glycan N343(B)   |
| B    | Ser49B, Arg346B, Phe347B, Ala348B, Val350B, Tyr351B, Ala352B, Trp353B, Leu371C, Ala372C, Phe374C, Phe400B, Val401B, Ile402B, Arg403B, Glu406B, Gly416B, Lys417B, Asn417B, Ile418B, Ala419B, Tyr421B, Asn422B, Tyr423B, Leu441B, Asp442B, Ser443B, Lys444B, Gly447B, Asn448B, Tyr449B, Asn450B, Tyr451B, Leu452B, Arg452B, Tyr453B, Arg454B, Leu455B, Phe456B, Arg457B, Leu461B, Thr470B, Glu471B, Tyr473B, Tyr489B, Phe490B, Pro491B, Leu492B, Gln493B, Arg493B, Ser494B, Tyr495B, Gly496B, Ser496B, Phe497B, Gln498B, Asn501B, Tyr501B, Tyr505B, His505B, Pro507B, Glycan N165(C), Glycan N343(C)   |
| C    | Asn370A, Ser371A, Ser373A, Phe377A, Lys378A, Cys379A, Tyr380A, Gly381A, Val382A, Ser383A, Pro384A, Thr385A, Lys386A, Ala411A, Pro412A, Gln414A, Asp427A, Asp428A, Phe429A, Thr430A, Gly431A, Leu517A, Tyr51C, Ser349C, Val350C, Ala352C, Ile402C, Arg403C, Glu406C, Gly416C, Asn417C, Lys417C, Ile418C, Ala419C, Asp420C, Tyr421C, Asn422C, Tyr423C, Tyr449C, Asn450C, Tyr451C, Leu452C, Arg452C, Tyr453C, Arg454C, Leu455C, Phe456C, Lys458C, Ser459C, Leu461C, Asp467C, Ile468C, Arg469C, Thr470C, Glu471C, Ile472C, Tyr473C, Gln474C, Ala475C, Glu484C, Cys488C, Tyr489C, Phe490C, Pro491C, Leu492C, Gln493C, Arg493C, Ser494C, Tyr495C, Gly496C, Ser496C, Phe497C, Tyr501C, Glycan N165(A), Glycan N343(A) |
| D    | Ser13C, Cys15C, Val16C, Leu18C, Ala67C, Val67C, Ile68C, His69C, Ser71C, Phe79C, Arg78C, Asn81C, Glu96C, Lys97C, Ser98C, Asn99C, Ile100C, Ile101C, Arg102C, Gly103C, Leu118C, Val120C, Asn121C, Asn122C, Pro139C, Ala123C, Thr124C, Asn125C, Val127C, Asp138C, Pro139C, Phe140C, Leu141C, Asp142C, Gly142C, Val143C, Tyr144C, Tyr145C, His146C, Lys147C, Asn148C, Asn149C, Lys150C, Ser151C, Trp152C, Met153C, Glu154C, Gly156C,  |

|   |   |
|---|---|
|   | Ser155C, Glu156C, Phe157C, Arg158C, Val159C, Phe175C, Leu176C, Met177C, Asp178C, Leu179C, Glu180C, Gly181C, Lys182C, Gln183C, Arg190C, Thr240C, Leu241C, Leu242C, Ala243C, Leu244C, His245C, His245C, Arg246C, Ser247C, Tyr248C, Leu249C, Thr250C, Ser254C, Gly257C, Trp258C, Thr259C, Ala260C, Gly261C, Ala262C, Ala263C, Glycan N122(C), Glycan N149(C)   |
| E | Asp420A, Tyr421A, Phe456A, Arg457A, Lys458A, Ser459A, Asn460A, Thr385B, Lys386B, Asn388B, Asp389B, Pro527B, Lys528B, Thr415A, Gly416A, Tyr473A, Asp364B, Ser366B, Gly526B, Lys529B, Tyr369B, Asn370B, Val367B, Leu455A, Leu461A, Leu387B, Tyr453A, Arg454A, Pro384B, Lys417A, Ile418A, Tyr489A, Asp985C, Tyr365B, Lys462A, Val327B, Lys424A, Pro463A, Leu371B, Glycan N234(B), Glycan N343(B), Glycan T323(B)   |
| F | Pro330B, Ile332B, Arg357B, Ile358B, Ser359B, Asn360B, Cys361B, Phe392B, Thr393B, Asn394B, Val395B, Tyr396B, Glu516B, Leu518B, His519B, Ala520B, Pro521B, Ala522B, Thr523B, Val524B, Asn544B, Leu560B, Pro561B, Phe562B, Gln563B, Gln564B, Arg577B, Leu582B, Lys41C, Ile128C, Phe168C, Glu169C, Tyr170C, Val171C, Ser172C, Gln173C, Pro174C, Phe175C, Tyr200C, Lys202C, Pro225C, Leu226C, Val227C, Asp228C, Leu229C, Pro230C, Glycan N331(B), Glycan N122(C)   |
| G | Ile119A, Thr124A, Asn125A, Val126A, Val127A, Ile128A, Phe168A, Glu169A, Tyr170A, Val171A, Ser172A, Gln173A, Pro174A, Phe175A, Leu179A, Ile203A, Leu226A, Val227A, Asp228A, Leu229A, Pro230A, Arg357C, Ser359C, Asn360C, Asn394C, Tyr396C, Thr523C, Glycan N122(A), Glycan N149(A), Glycan N331(C),  |
| H | Arg357A, Ser359A, Asn360A, Thr393A, Asn394A, Ala520A, Pro521A, Ala522A, Thr523A, Pro561A, Phe562A, Lys41B, Leu117B, Ile119B, Val120B, Asn121B, Thr124B, Asn125B, Val126B, Val127B, Ile128B, Lys129B, Val130B, Phe168B, Glu169B, Tyr170B, Val171B, Ser172B, Gln173B, Pro174B, Phe175B, Leu176B, Met177B, Leu179B, Phe192B, Tyr200B, Phe201B, Lys202B, Ile203B, Tyr204B, Ser205B, Glu224B, Pro225B, Leu226B, Val227B, Asp228B, Leu229B, Pro230B, Ile231B, Gly232B, Glycan N331(A), Glycan N122(B), Glycan N282(B)                             |
| I | Ser325A, Val327A, Val382A, Ser383A, Thr385A, Lys386A, Leu387A, Asn388A, Asp389A, Leu390A, Leu518A, Lys528A, Asn540A, Phe541A, Asn542A, Gly545A, Leu546A, Thr547A, Gly548A, Glu748B, Asn978B, Ile980B, Leu981B, Ser982B, Arg983B, Leu984B, Asp985B, Lys986B, Ala989B, Thr747B, Asp979B, Ser746B, Phe329A, Leu977B, Phe543A, Asn544A, Thr549A, Val976B, Ile326A, Val987B, Glu988B, Ile993B, Pro322A, Glu324A, Asp745B, Lys417C, Gln321A, Thr323A, Val539A, Lys547A, Phe981B, Arg328A, Gly550A, Glucan T323(A), Glycan S325(A), Glycan N234(A) |
| J | Gln52B, Thr274B, Gln271B, Arg273B, Asp290B, Cys291B, Ala292B, Leu293B, Glu298B, Ser316B, Asn317B, Phe318B, Arg319B, Val320B, Gln321B, Pro322B, Thr323B, Glu324B, Lys537B, Cys538B, Asn540B, Thr549B, Val551B, Cys590B, Ser591B, Phe592B, Gly593B, Val595B, Tyr612B, Glu619B, Val620B, Pro621B, Val622B, Ala623B, Ile624B, His625B, Ala626B, Asp627B, Gln628B, Leu629B, Thr630B, Pro631B, Thr632B, Trp633B, Arg634B, Val635B, Met740C, Asp745C, Thr747C, Glycan N234(B), Glycan T323(B)  |

|   |  |
|---|--|
| K | Asp737A, Cys738A, Thr739A, Met740A, Ile742A, Cys743A, Gly744A, Asp745A, Ser746A, Thr747C, Glu748A, Cys749A, Ser750A, Asn751A, Leu752A, Leu753A, Leu754A, Gln755A, Tyr756A, Phe759A, Gly757A, Ser758A, Cys760A, Thr761A, Lys764A, Ile993A, Ile997A, Leu1001A, Ser50C, Gln52C, Asp53C, Pro272C, Thr274C, Glu298C, Lys304C, Ser316C, Asn317C, Phe318C, Arg319C, Thr302C, Phe592C, Thr630C, Glycan N234(C)   |
| L | Leu24B, Pro25B, Pro26B, Ala27B, Tyr28B, Thr29B, Asn30B, Asn61B, Val62B, Thr63B, Trp64B, Phe65B, His66B, Ile68B, Val70B, Arg78B, Val213B, Arg214B, Asp215B, Tyr266B, Leu212B, ins-Glu2141B, ins-Pro2142B, ins-Glu2143B, Glycan N61(B), Glycan N74(B), Glycan N603(B)  |
| M | Val47B, Leu48B, His49B, Ser50B, Thr51B, Gln52B, Thr274B, Leu276B, Val289B, Cys291B, Pro295B, Ser297B, Glu298B, Thr299B, Lys300B, Cys301B, Thr302B, Leu303B, Lys304B, Ser305B, Phe306B, Thr307B, Val308B, Tyr313B, Gln314B, Thr315B, Ser316B, Asn317B, Phe318B, Ile569A, Trp633B, Arg634B, Cys738C, Thr739C, Leu753C, Leu754C, Tyr756C, Gly757C, Ser758C, Phe759C, Cys760C, Thr761C, Gln762C, Leu763C, Lys764C, Asn764C, Arg765C, Gln957B, Asn960B, Thr961B, Lys964B, Gln965B, Ser968B, Ser967B,  |
| N | Leu48A, His49A, Ser50A, Thr51A, Thr274A, Phe275A, Leu276A, Leu277A, Val289A, Cys291A, Ser297A, Glu298A, Thr299A, Lys300A, Cys301A, Thr302A, Leu303A, Lys304A, Ser305A, Phe306A, Thr315A, Thr961A, Lys964A, Leu754B, Gly757B, Ser758B, Cys760B, Thr761B, Asn764B, Gln52A, Leu296A, Ser316A, Arg765B, Asp290A, Ala292A, Phe759B, Gln762B, Thr739B, Leu753B, Val308A, Asp294A, Pro295A, Gln314A, Thr307A, Gln957A, Gln755B, Tyr756B, Tyr313A, Val597A, Gln965A, Cys738B, Lys764B, Asn317A, Phe318A, Ile569C, Leu849A, Glycan N234(A), Glycan T323(A)  |
| O | Ile834A, Ile312C, Val595C, Ser596C, Ile598C, Val608C, Ala609C, Val610C, Leu611C, Tyr612C, Gln613C, Gly614C, Val615C, Asn616C, Cys617C, Thr618C, Glu619C, Val620C, Pro621C, Val622C, Ala623C, Ile624C, Leu629C, Thr630C, Pro631C, Thr632C, Trp633C, Arg634C, Val635C, Tyr636C, Ser637C, Thr638C, Gly639C, Ser640C, Asn641C, Val642C, Phe643C, Gln644C, Thr645C, Arg646C, Ala647C, Gly648C, Cys649C, Leu650C, Ile651C, Gly652C, Ala653, Glu654C, His655C, Tyr655C, Val656C, Ile666C, Ile670C, Cys671C, Ala672C, Gln675C, Arg682C, Arg683C, Ser686C, Ala688C, Ser689C, Gln690C, Ser691C, Ile692C, Ile693C, Ala694C, Tyr695C, Glycan N616(C), Glycan N657(C) |
| P | Asn616B, Gln644B, Thr645B, Arg646B, Ala647B, Gly648B, Ala668B, Gly669B, Ile670B, Pro812C, Ser813C, Lys814C, Arg815C, Phe823C, Leu828C, Ala829C, Asp830C, Ala831C, Gly832C, Phe833C, Ile834C, Lys835C, Gln836C, Tyr837C, Pro862C, Pro863C, Leu865C, Thr866C, Asp867C, Glu868C, Met869C, His1058C, Glycan N616(B), Glycan N657(B), Glycan N282(C)  |
| Q | Ala609A, Val610A, Leu611A, Tyr612A, Val615A, Asn616A, Cys617A, Thr618A, Glu619A, Val620A, Pro621A, Leu629A, Thr632A, Gly639A, Ser640A, Asn641A, Val642A, Phe643A, Gln644A, Thr645A, Gly648A, Cys649A, Leu650A, Ile651A, Gly652A, Ala653A, Glu654A, His655A, Val656A, Ile670A, Arg682A, Ala694A, Thr630A, Arg646A, Gln628A, Ile666A, His655A, Arg634A, Asn657A, Arg681A, Arg683A, Ile693A, Tyr695A, Thr638A, His625A, Thr696A, Ala623A, Ser686A, Ser691A, Ile692A, Tyr655A, Glycan N616(A), Glycan N657(A)  |



|   |  |
|---|--|
| R | Leu1024A, Thr1027A, Lys1028A, Glu1031A, Ser1037A, Lys1038A, Arg1039A, Val1040A, Asp1041A, Phe1042A, Cys1043A, Glu780B, Val781B, Gln784B, Ala1020B, Ser1021B, Ala1022B, Asn1023B, Leu1024B, Ala1025B, Ala1026B, Thr1027B, Lys1028B, Met1029B, Ser1030B, Glu1031B, Cys1032B, Val1033B, Leu1034B, Ser1037B, Arg1039B, Phe1042B, Thr1027C, Glu1031C, Arg1039C, Cys1032A, Leu727B, Cys1043B, Gly1035B, Phe1062B, Trp886B, Asn1023C, Ser1030C, Gln1036B, Lys1038B, His1064B, Phe1042C, Gly1044A, Lys1045A, Glu725A |
| S | Val722C, Gly799C, Phe800C, Asn801C, Phe802C, Ser803C, Gln804C, Ile805C, Gln920C, Lys921C, Leu922C, Ile923C, Ala924C, Asn925C, Gln926C, Phe927C, Asn928C, Ser929C, Ala930C, Ile931C, Gly932C, Lys933C, Ile934C, Gln935C, Asp936C, Glycan N709 (B), Glycan N717(C), Glycan N801(C)   |

**Table S4:** Fraction of each group measured by mass photometer for Omicron ternary complex with or without heparan sulfate.

| Group<br>Sample              | A<br>(fraction) | B<br>(fraction) | C<br>(fraction) |
|------------------------------|-----------------|-----------------|-----------------|
| Omicron + ACE2               | 0.448           | 0.215           | 0.337           |
| Omicron + ACE2               | 0.453           | 0.240           | 0.307           |
| Omicron + ACE2               | 0.428           | 0.236           | 0.336           |
| Average (Standard Deviation) | 0.443 (0.014)   | 0.230 (0.013)   | 0.327 (0.017)   |
| Group<br>Sample              | A<br>(fraction) | B<br>(fraction) | C<br>(fraction) |
| Omicron + HS + ACE2          | 0.468           | 0.395           | 0.137           |
| Omicron + HS + ACE2          | 0.349           | 0.469           | 0.181           |
| Omicron + HS + ACE2          | 0.316           | 0.488           | 0.195           |
| Average (Standard Deviation) | 0.378 (0.080)   | 0.451 (0.050)   | 0.171 (0.030)   |

**Table S5:** Fraction of each group measured by mass photometer for Delta ternary complex with or without heparan sulfate.

| Sample \ Group               | A (fraction)  | B (fraction)  | C (fraction)  |
|------------------------------|---------------|---------------|---------------|
| Delta + ACE2                 | 0.447         | 0.147         | 0.406         |
| Delta + ACE2                 | 0.438         | 0.152         | 0.409         |
| Delta + ACE2                 | 0.421         | 0.174         | 0.405         |
| Average (Standard Deviation) | 0.435 (0.013) | 0.158 (0.014) | 0.407 (0.002) |
| Sample \ Group               | A (fraction)  | B (fraction)  | C (fraction)  |
| Delta + HS + ACE2            | 0.507         | 0.145         | 0.348         |
| Delta + HS + ACE2            | 0.473         | 0.155         | 0.372         |
| Delta + HS + ACE2            | 0.545         | 0.191         | 0.264         |
| Average (Standard Deviation) | 0.508 (0.036) | 0.163 (0.024) | 0.328 (0.057) |

**Table S6:** Fraction of each group measured by mass photometer for WT ternary complex with or without heparan sulfate.

| Sample \ Group               | A (fraction)  | B (fraction)  | C (fraction)  |
|------------------------------|---------------|---------------|---------------|
| WT + HS + ACE2               | 0.573         | 0.312         | 0.115         |
| WT + HS + ACE2               | 0.697         | 0.224         | 0.079         |
| WT + HS + ACE2               | 0.597         | 0.254         | 0.150         |
| Average (Standard Deviation) | 0.622 (0.066) | 0.263 (0.045) | 0.115 (0.035) |
| Sample \ Group               | A (fraction)  | B (fraction)  | C (fraction)  |
| WT + HS + ACE2               | 0.517         | 0.336         | 0.147         |
| WT + HS + ACE2               | 0.641         | 0.209         | 0.150         |
| WT + HS + ACE2               | 0.553         | 0.276         | 0.171         |
| Average (Standard Deviation) | 0.570 (0.064) | 0.274 (0.064) | 0.156 (0.013) |

**Table S7:** Comparison of the limit of detection for spike protein detection in lateral flow assay

| Target | Bioreceptor                          | Detection type | Limit of Detection (ng/reaction) | Ref.                  |
|--------|--------------------------------------|----------------|----------------------------------|-----------------------|
| Spike  | Primary: ACE2<br>Secondary: Antibody | sandwich-type  | 5 ng/reaction<br>(buffer)        | Lee2020 <sup>42</sup> |

---

|       |   |               |                  |                         |
|-------|---|---------------|------------------|-------------------------|
|       | Primary: NeuNAc <sup>a</sup>                          |               |                  |                         |
| Spike | Secondary: NueNAc-<br>PHEA <sub>50</sub> <sup>b</sup> | sandwich-type | 200 ng/reaction  | Baker2020 <sup>43</sup> |
|       | Primary: ACE2   |               | 1 ng/reaction    |                         |
| Spike | Secondary: Antibody                                   | sandwich-type | (buffer)         | Lee2022 <sup>44</sup>   |
|       | Primary: Heparin                                      |               | 19.5 ng/reaction |                         |
| Spike | Secondary: NTD Ab                                     | sandwich-type | (buffer)         | Kim2022 <sup>22</sup>   |
|       | Primary: Heparin                                      |               | 78 ng/reaction   |                         |
| Spike | Secondary: ACE2                                       | Sandwich-type | (saliva)         |                         |
|       | Primary: Heparin                                      |               | 10 ng/reaction   |                         |
|       | Secondary: ACE2                                       |               | (buffer)         |                         |
|       |   |               | 20 ng/reaction   | In this study           |
|       |   |               | (saliva)         |                         |

---

**Figures:**

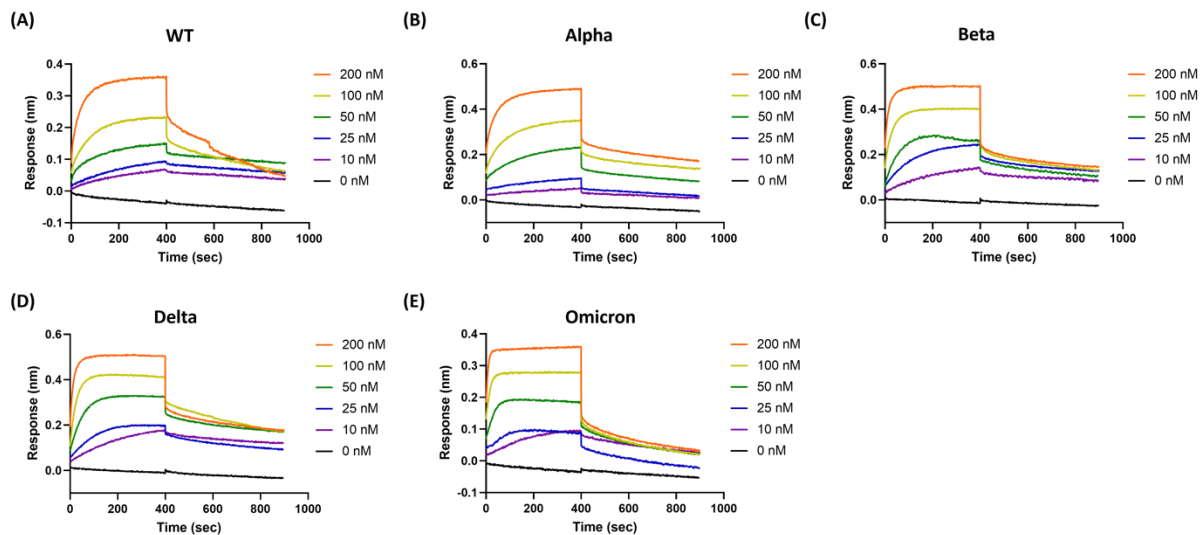


**Figure S1:** BLI sensogram of the ACE2 binding to variant of SARS-CoV-2 spike proteins (A) Wild type, (B) Alpha, (C) Beta, (D) Delta, and (E) Omicron. ACE2 binding to 0, 10, 25, 50, 100, 200 nM of spike proteins for each variant were measured. Control sample (0 nM) was subtracted to analyze the binding affinity using the steady-state analysis.

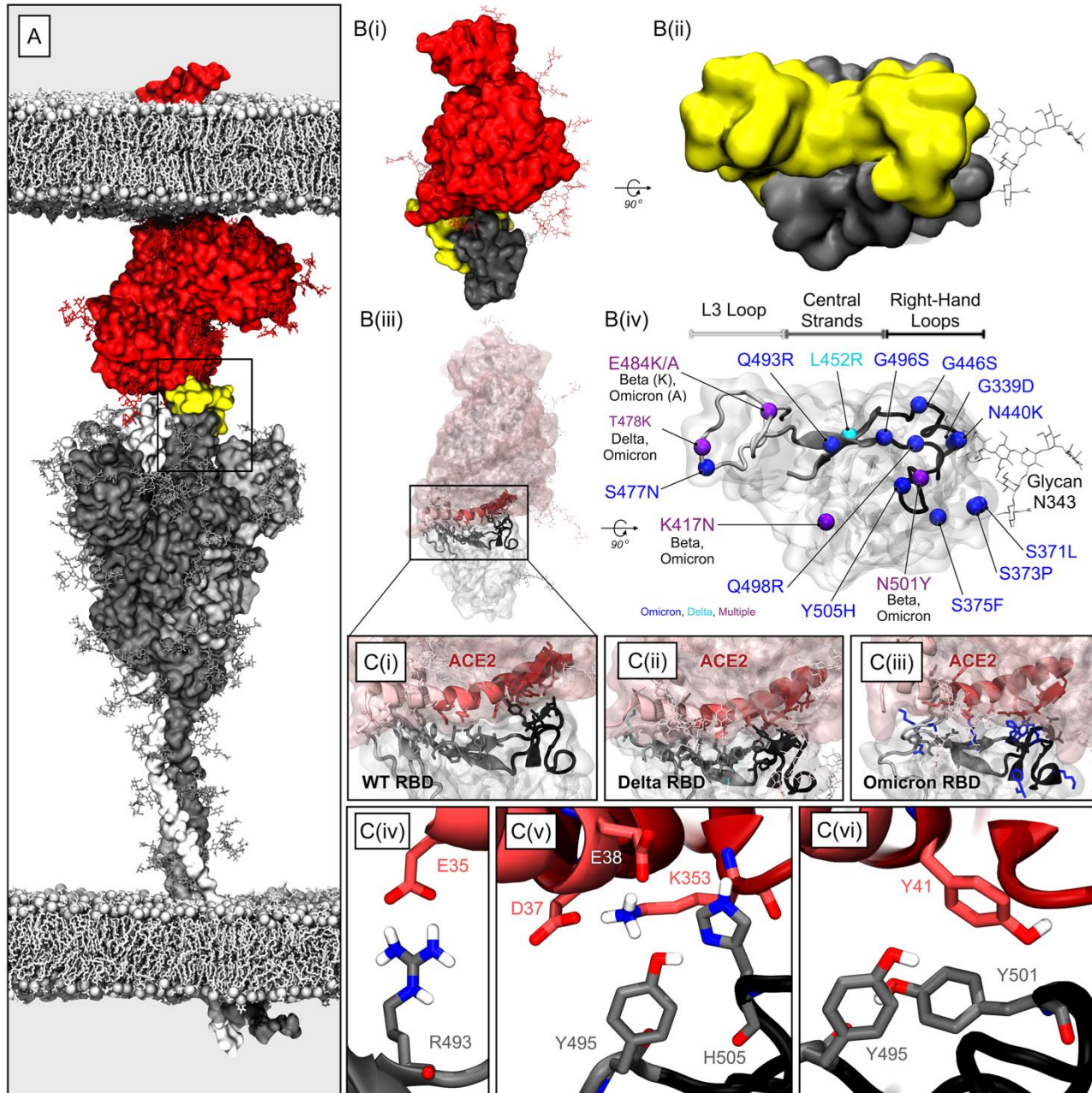


**Figure S2:** Image of (A) the spike/ACE2 double membrane complex.<sup>44</sup> ACE2 shown in dark red surface representation, ACE2 glycans shown in dark red licorice; SARS-CoV-2 spike protein in 1up conformation is shown in a grey surface representation (chain A as dark grey, chain B as light grey, chain C as white), the spike's exposed RBM is highlighted with a yellow surface, spike glycans shown in grey licorice; human and SARS-CoV-2 membranes are shown in grey licorice representation with phosphorous atoms represented in VDW. A rectangular box outlines the ACE2+RBM interface. (B(i)) Image showing the ACE2+RBD system constructed in this work for MD simulations. All molecules colored and represented as described in panel A. (B(ii)) Spike RBD with RBM highlighted. Spike RBD in grey surface representation, RBM highlighted in yellow. N-linked glycan at N343 shown in grey licorice representation. (B(iii)) Same system as shown in B(i) but with transparent surfaces to highlight the secondary

structure at the ACE2+RBD interface. ACE2 surface is shown in transparent red, with ACE2 glycans shown in pink licorice, spike RBD surface is shown in transparent grey with glycan N343 shown in grey licorice. The RBD side of the ACE2+RBD interface is represented in opaque ribbons and colored in shades of grey; the L3 Loop (residues 470-489), central beta strands (residues 450-456, 490-496), and right-handed loops (residues 438-450, 497-508) are colored as light grey, grey, and black ribbons, respectively. The ACE2 side of the ACE2+RBD interface is composed largely of one N-terminal alpha helix (residues 18-50), a neighboring helix (residues 82-83), and a neighboring beta-strand (residues 353-357). ACE2 residues within the ACE2+RBD interface that interact primarily with the RBD L3 loops, RBD central beta strands, and RBD right-handed loops are represented as pink, red, and dark red ribbons, respectively. A callout box highlights the ACE2+RBD interface. (B(iv)) Spike RBD shown in same orientation as shown in B(ii) but with transparent surface to reveal the positions of mutations in Beta, Delta, and Omicron BA.1 SARS-CoV-2 variant spike sequences. The L3 Loop, central beta strands, and right-handed loops are represented as in B(iii). Positions of mutations seen in the Delta and Omicron spike sequences are shown as cyan and blue beads, respectively, while positions of mutations seen in multiple spike sequences are shown as purple beads with denotation of sequence. Glycan N343 is represented in grey licorice. (C(i-iii)) Visualization of WT, Delta, and Omicron RBDS bound to ACE2. Secondary structural elements at the ACE2+RBD interface are represented in panels B(iii) and B(iv). Cyan and blue residues indicate positions of mutation within the Delta and Omicron spike sequences, respectively. (C(iv-vi)) Zoom-in images highlighting specific interactions of high interest observed in ACE2+Omicron spike RBD simulations as discussed in the main text. Red carbon atoms denote ACE2 residues, grey carbon atoms denote Omicron RBD residues.

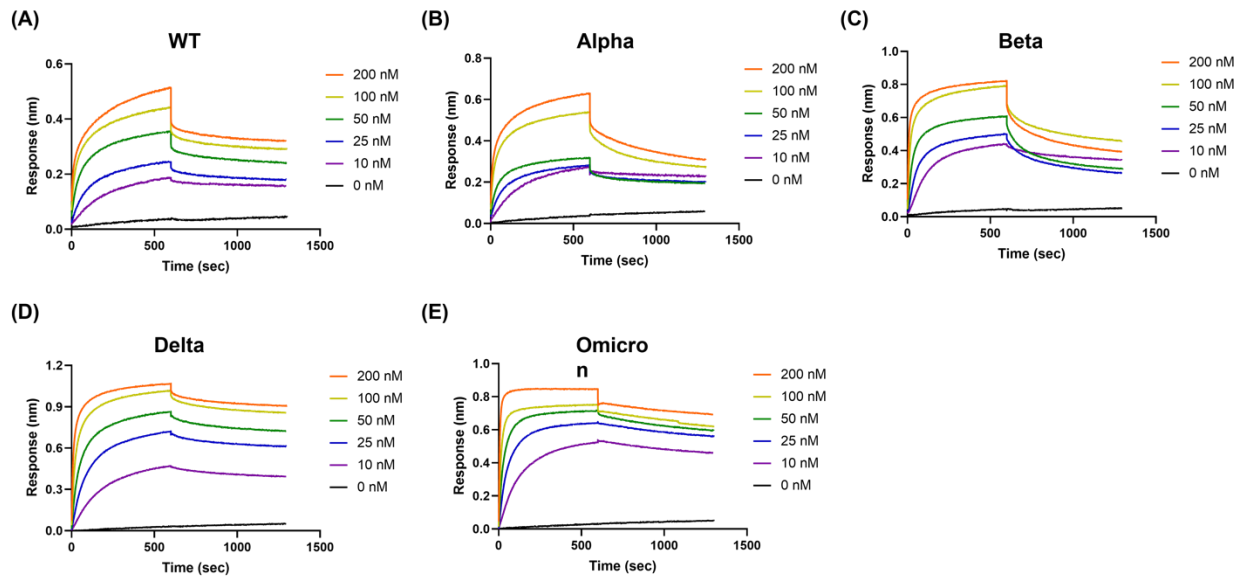


**Figure S3:** BLI sensogram of the heparin (HEP) binding to variant of SARS-CoV-2 spike proteins (A) Wild type, (B) Alpha, (C) Beta, (D) Delta, and (E) Omicron. HEP binding to 0, 10, 25, 50, 100, 200 nM of spike proteins for each variant were measured. Control sample (0 nM) was subtracted to analyze the binding affinity using the steady-state analysis.



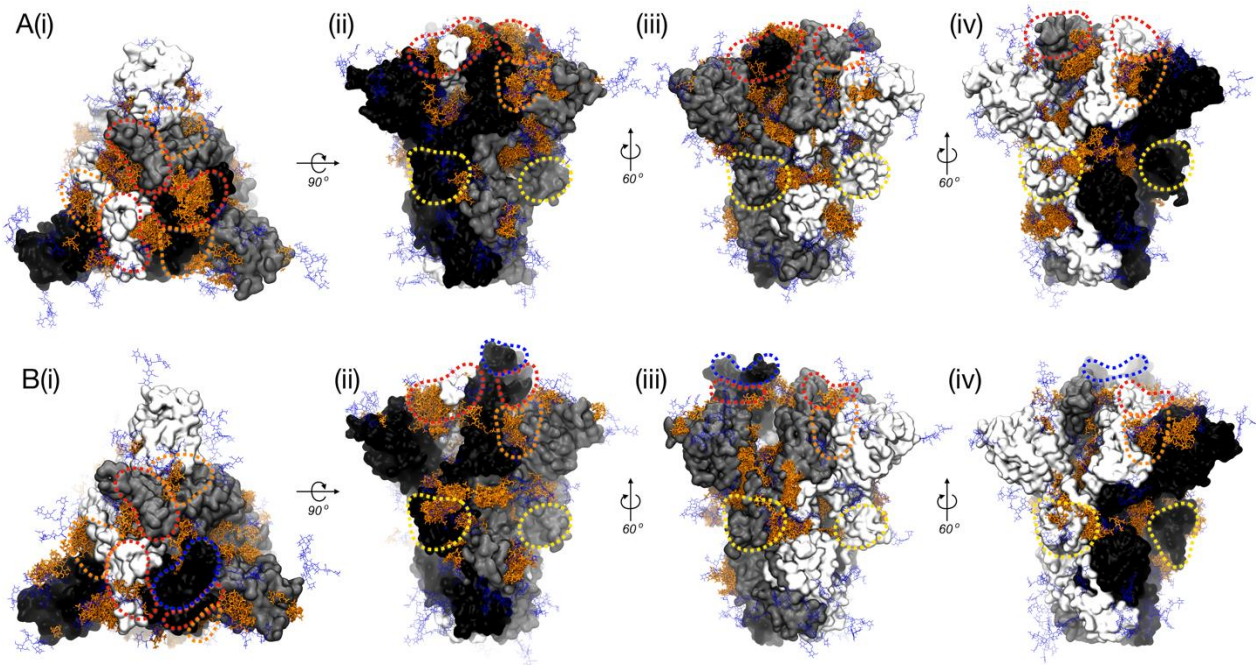


**Figure S4:** AutoDock Vina docking results illustrating heparin dimeric and tetrameric models bound to WT (A) closed and (B) 1-up structures. In all structures, spike chains A, B, and C are shown in black, grey, and white surface representations. Spike glycans are shown in thin blue licorice. Heparin dimeric and tetrameric binding modes are shown in orange licorice. Subpanels (i-iv) each represent the same structure in a different orientation. In all images, red, orange, yellow, and blue dotted lines highlight the RBD patch, RBD cleft, FCS, and RBM sites respectively.

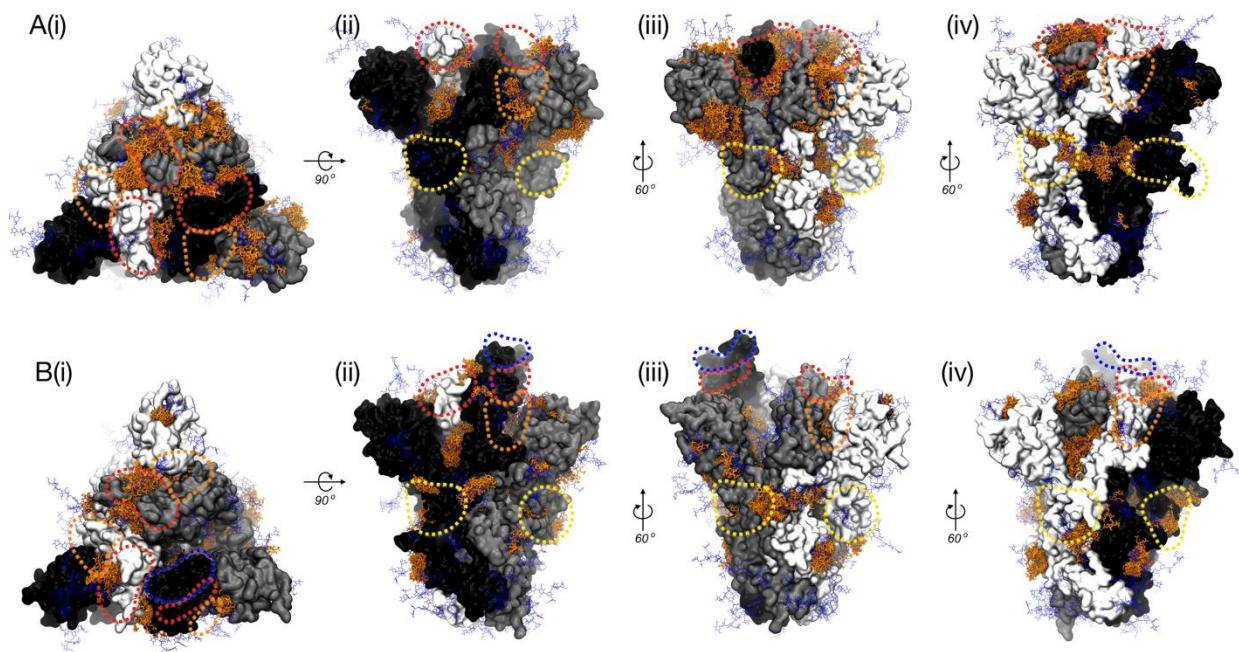


**Figure S5:** AutoDock Vina docking results illustrating heparin dimeric and tetrameric models bound to Delta (A) closed and (B) 1-up structures. In all structures, spike chains A, B, and C are shown in black, grey,

and white surface representations. Spike glycans are shown in thin blue licorice. Heparin dimeric and tetrameric binding modes are shown in orange licorice. In all images, red, orange, yellow, and blue dotted lines highlight the RBD patch, RBD cleft, FCS, and RBM sites respectively.

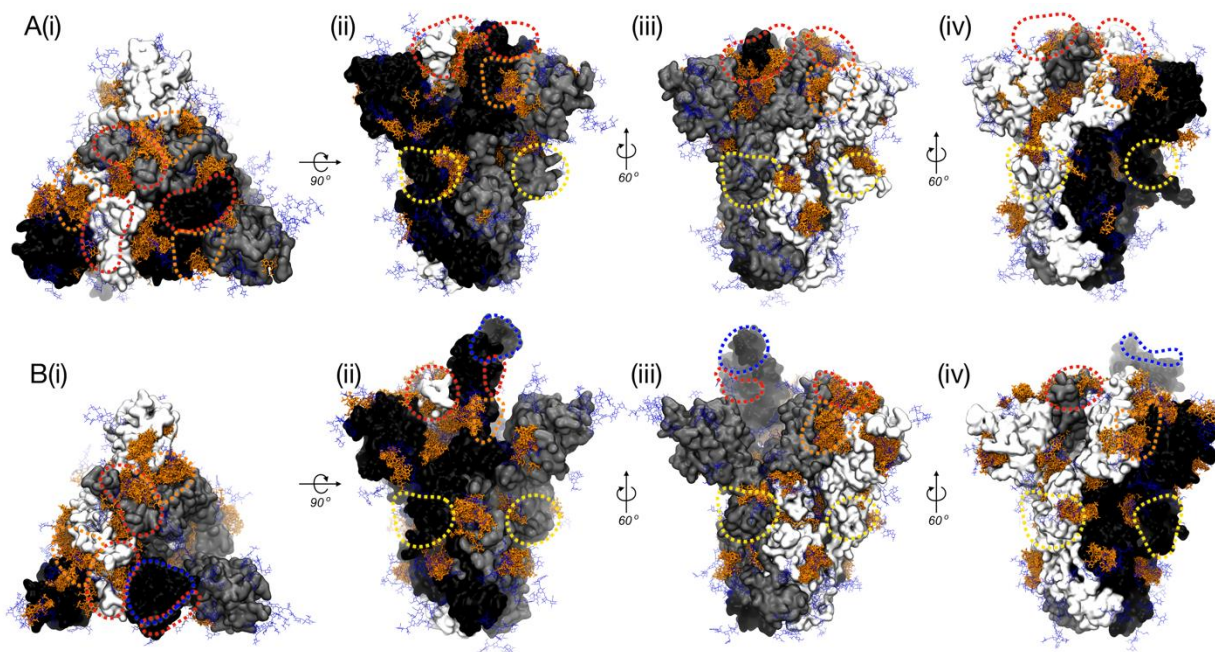


**Figure S6:** AutoDock Vina docking results illustrating heparin dimeric and tetrameric models bound to Omicron (A) closed and (B) 1-up structures. In all structures, spike chains A, B, and C are shown in black, grey, and white surface representations. Spike glycans are shown in thin blue licorice. Heparin dimeric and tetrameric binding modes are shown in orange licorice. In all images, red, orange, yellow, and blue dotted lines highlight the RBD patch, RBD cleft, FCS, and RBM sites respectively.

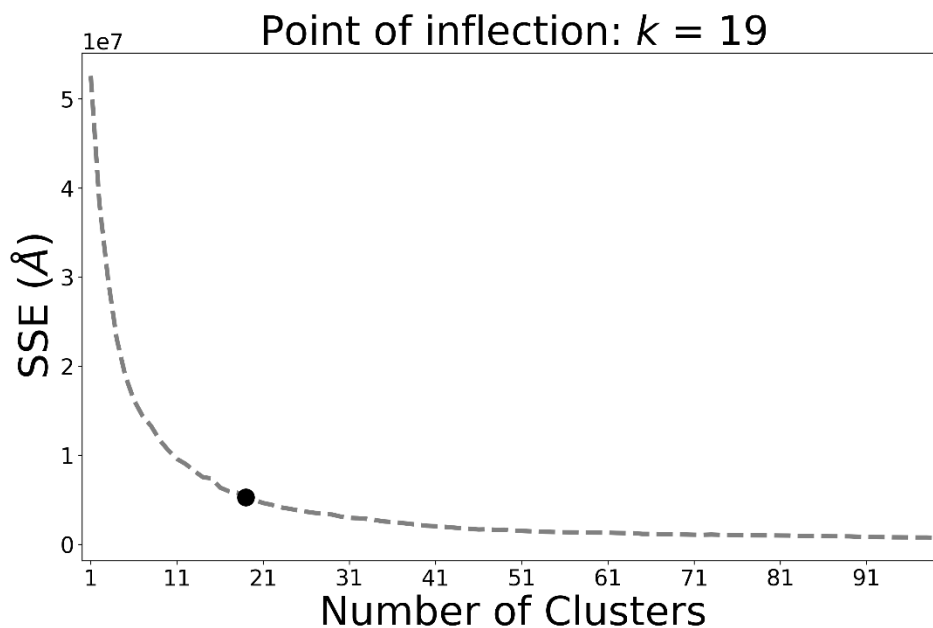




**Figure S7:** K-means clustering results determining the optimal number of clusters from 28,800 AutoDock vina binding modes.

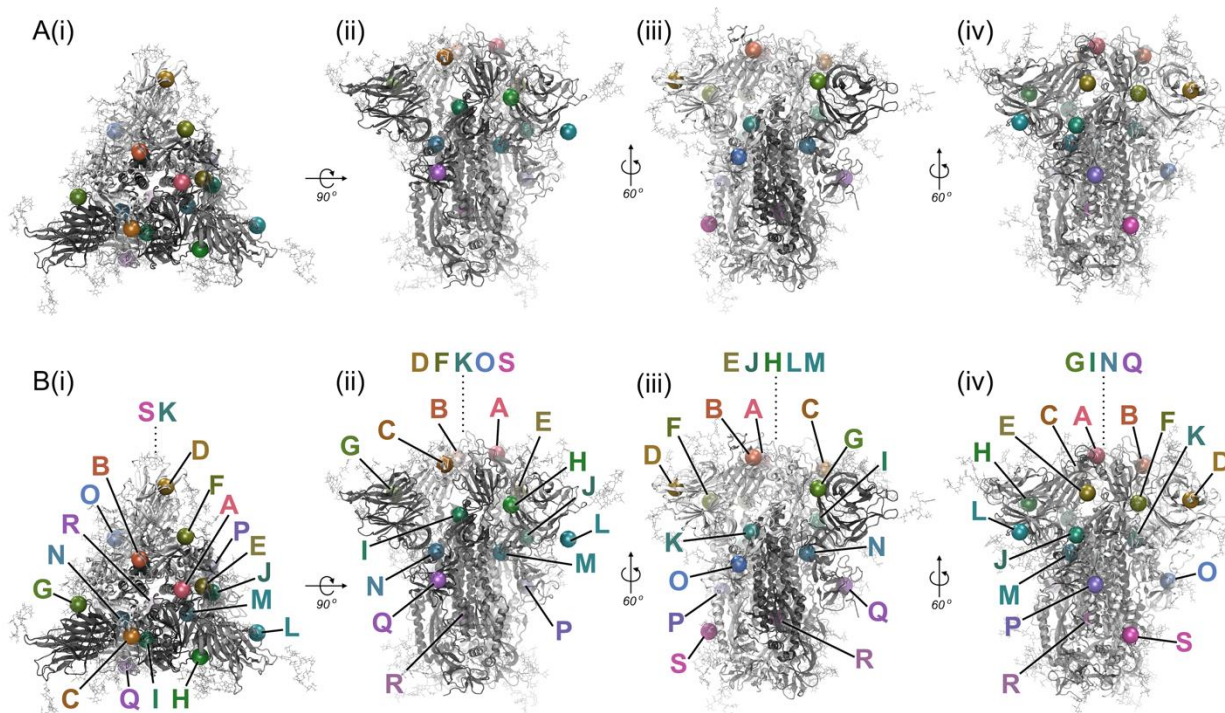


**Figure S8:** All 19 heparin hotspots found via ensemble-based docking with AutoDock and kmeans clustering. (A) Panels (i-iv) show the WT spike protein in closed conformation; chains A, B, and C are represented in grey, light grey, and white ribbons, respectively, and spike glycans are represented in light grey licorice. The centroid of each identified “hotspot” is represented with a 5 Å sphere. The hotspots were ordered by height on the spike protein (i.e., according to z-coordinate) and colored according to a rainbow color palette. All images are based on an identical structure and VMD scene but rotated to give complete viewing of spike apex (i) and three sides (ii-iv). (B) Panels (i-iv) show the same WT spike protein in closed conformation with the same representation scheme as in (A), but with each identified binding hotspot labeled according to its name A-R. Hotspots were named as described in Supporting Information methods. Sites not visible in a given orientation, due to rotation or fog in the image, are denoted with a dashed line.



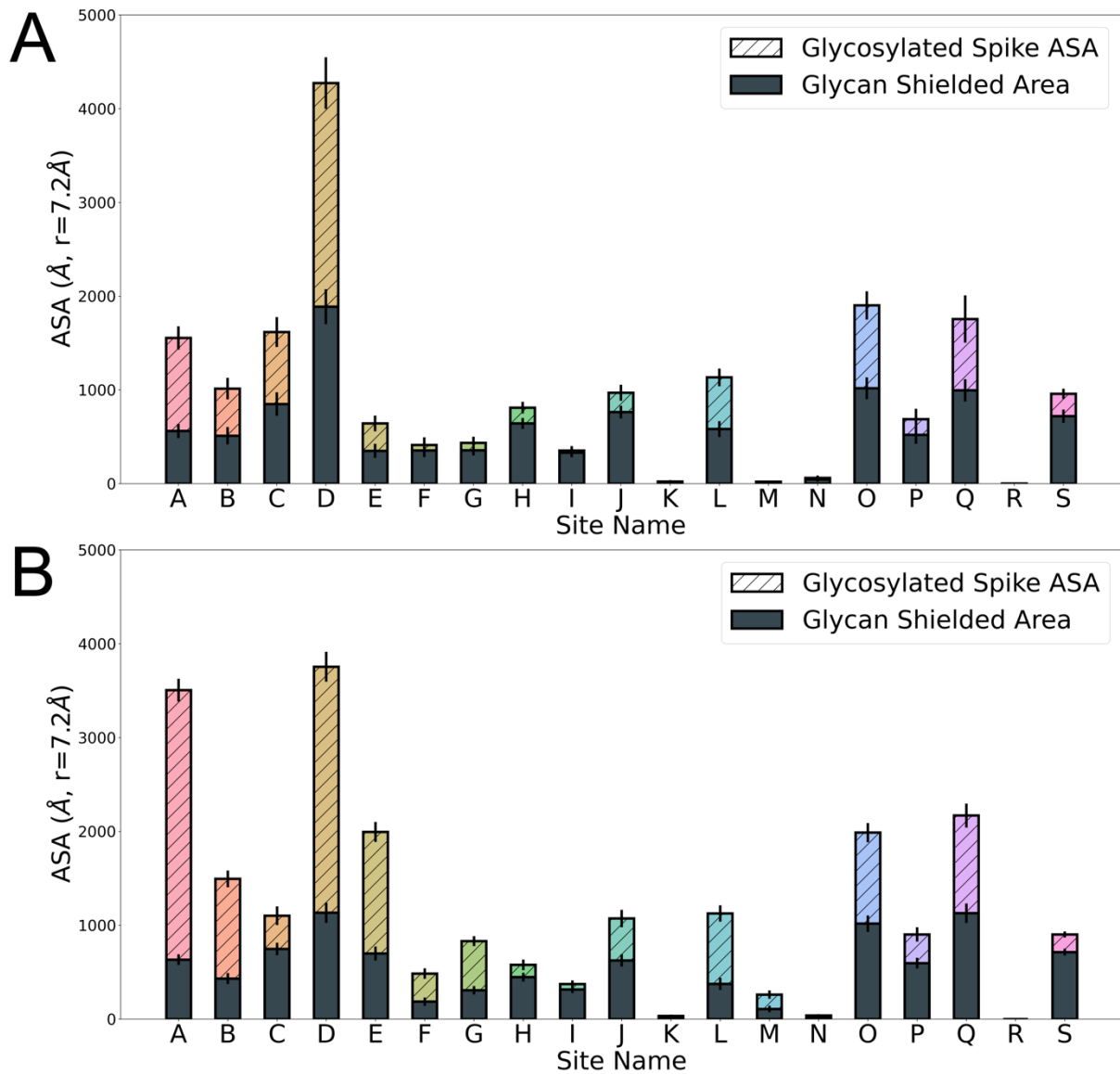


**Figure S9:** Accessible Surface Area plotted for each site calculated with a probe radius of  $7.2 \text{ \AA}$ , calculated according to the Shrake-Rupley algorithm. (A) ASAs calculated for each binding site from wild type spike simulations in the all-RBDs-down/closed conformation. (B) ASAs calculated for each binding site from wild type spike simulations in the 1-up RBD conformation.

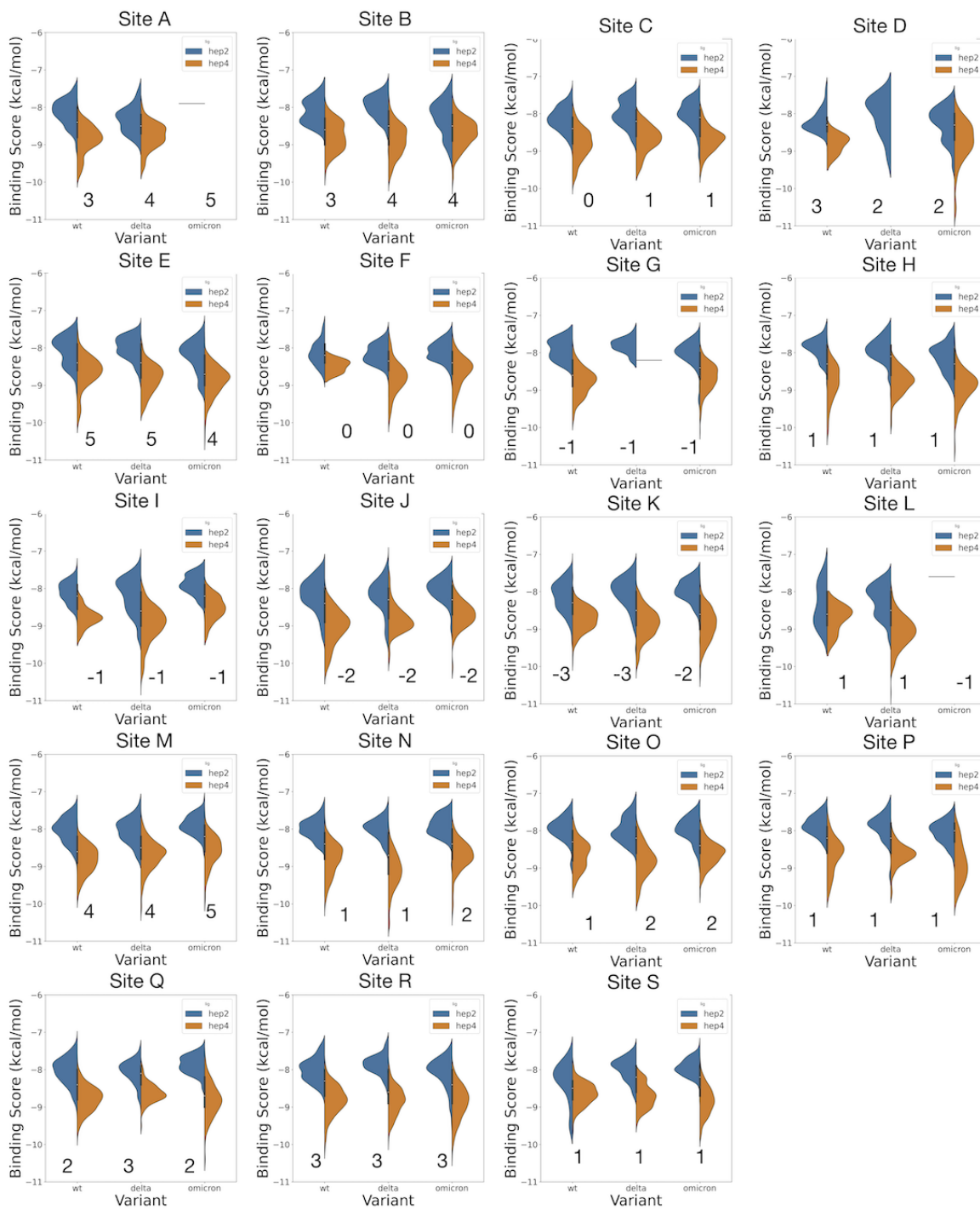


**Figure S10:** Violin plots demonstrating distribution of AutoDock Vina binding scores for heparin dimer (hep2) and tetramer (hep4) models each binding hotspot across all variants. Total charge per site per variant is denoted next to each violin within the plot. Site based distributions of AutoDock Vina binding scores were taken from both closed and 1up spike conformations per variant within each site.

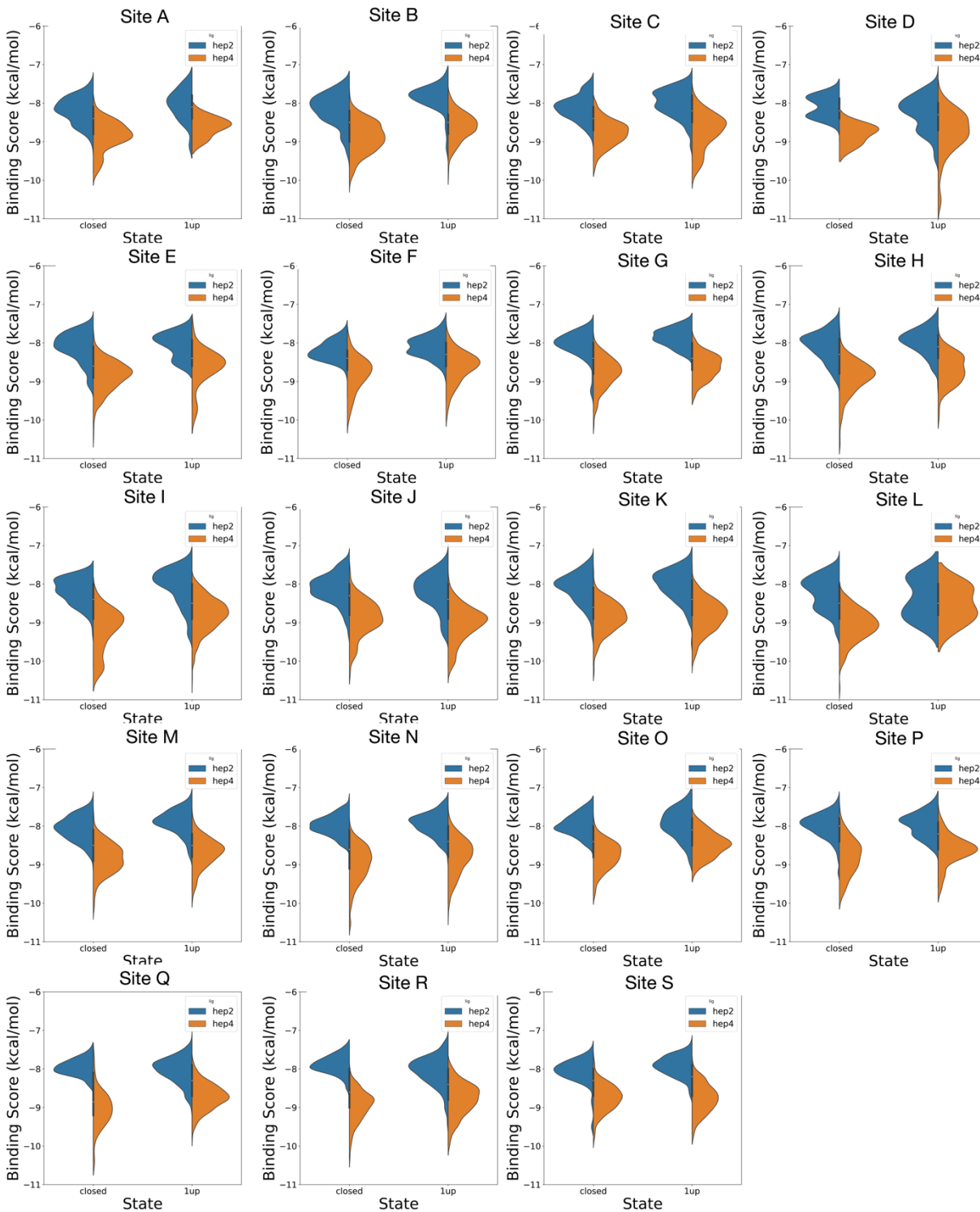


**Figure S11:** Violin plots demonstrating distribution of AutoDock Vina binding scores for heparin dimer (hep2) and tetramer (hep4) models each binding hotspot across 1up and closed spike structures. Site based distributions of AutoDock Vina binding scores were taken from all three spike variants (WT, Delta, and Omicron) per spike conformation.

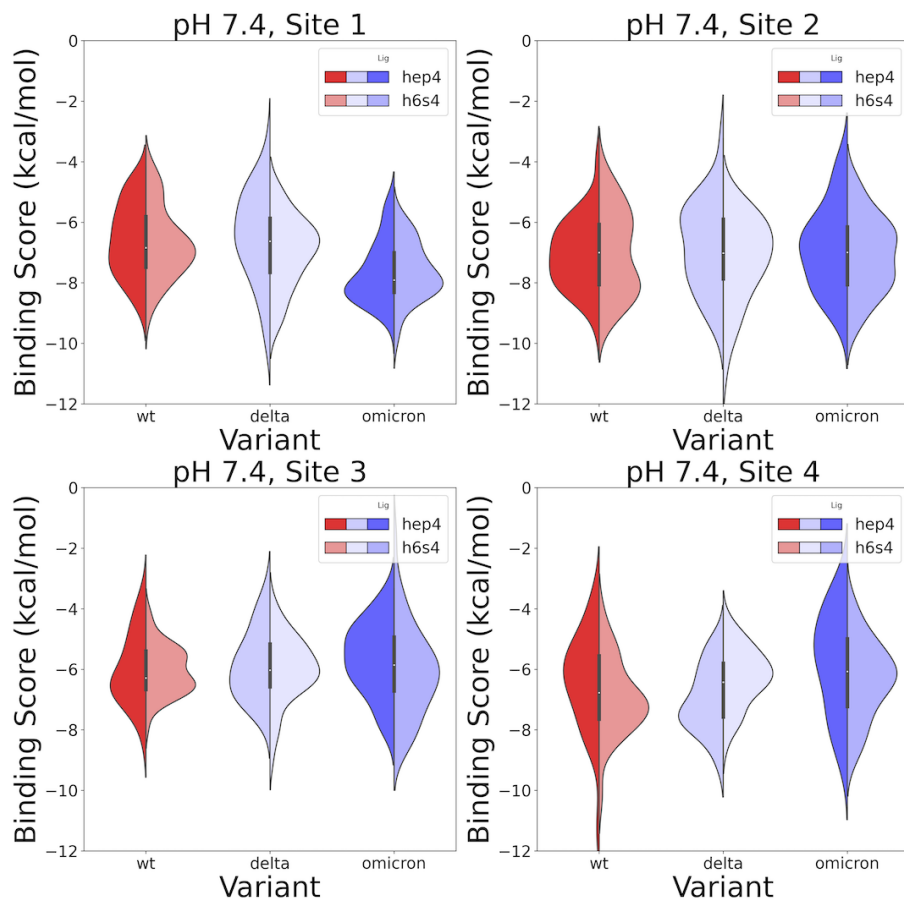


**Figure S12:** Violin plots illustrating the distribution of binding scores predicted by Schrodinger's Induced Fit Docking protocol in each of the probed sites, for each of the Variants, at pH's 7.4. Site 1 is the RBD Cleft Site, Site 2 is the RBD Patch Site, Site 3 is the Furin Cleavage Site, and Site 4 is the Receptor Binding Motif.

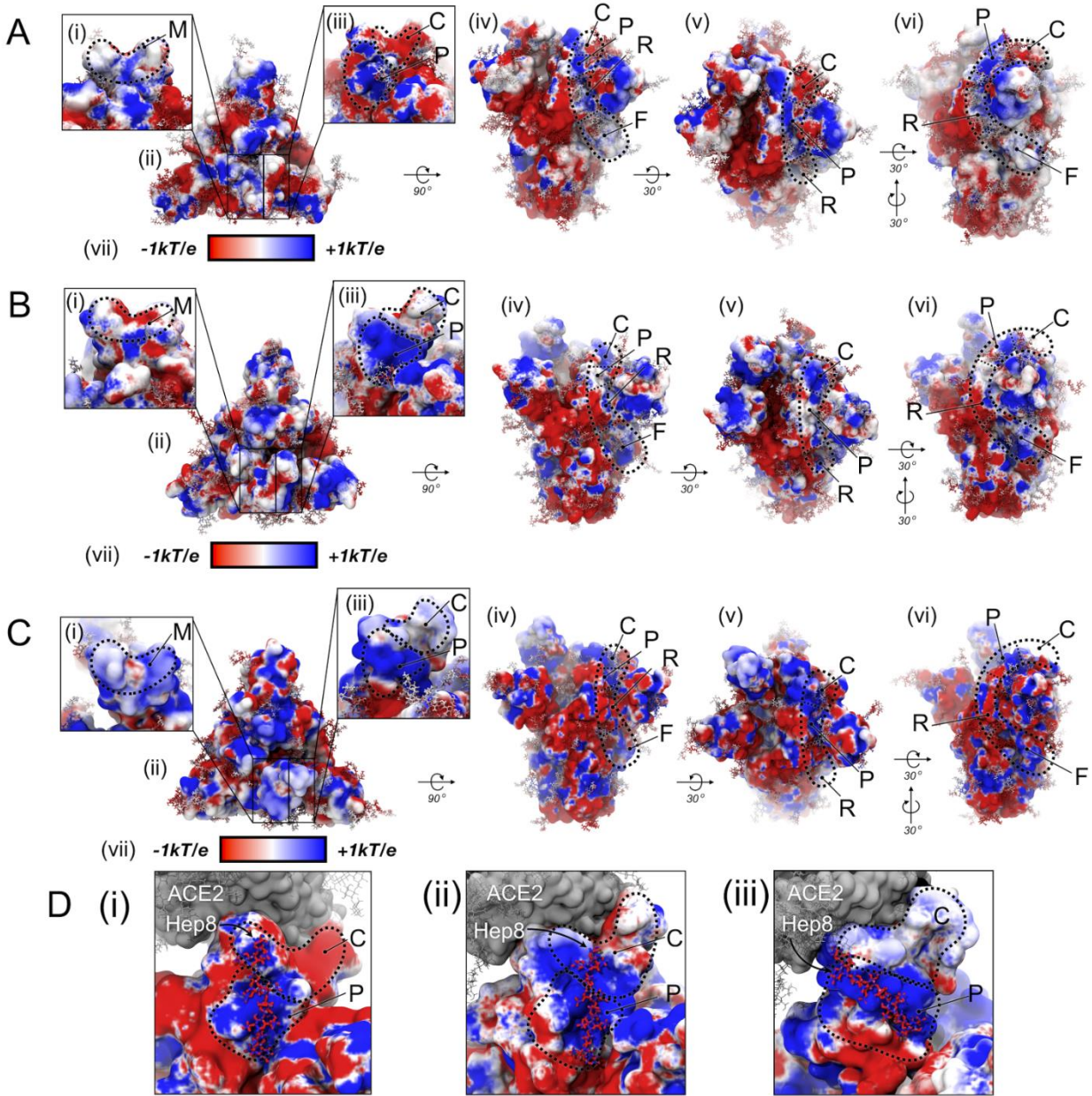


**Figure S13:** Dynamically-averaged electrostatic potential maps collected from 50 ns of MD simulations for (A) WT, (B) Delta, and (C) Omicron spike proteins in the 1up RBD conformation. For images A-C, labels (i-vii) indicate the following images: a close-up view of the RBM site (denoted as M), a top-down view of the spike protein, a close-up view of the RBD Cleft and RBD Patch sites (denoted as C and P, respectively), a side view of the spike protein with RBD Cleft, RBD Patch, Connecting Ridge, and FCS sites (denoted as C, P, R, and F, respectively) highlighted, a tilted-top-down view of the spike protein with RBD Cleft, RBD Patch, and Connecting Ridge sites (denoted as C, P, and R, respectively) highlighted, a rotated-side view of the spike protein with RBD Cleft, RBD Patch, Connecting Ridge, and FCS sites (denoted as C, P, R, and F, respectively) highlighted, and a color bar demonstrating the color ranges for each image and the corresponding calculated electrostatic potential. In all panels, protein surfaces are colored according to average electrostatic potential at each site, ranging from  $-1 k_B T/e$  (red) to  $+1 k_B T/e$  (blue). (D) Images demonstrating how the SARS-CoV-2 spike can, in the 1up state, accommodate binding of ACE2 (grey surface) at the RBM and a heparin octamer (Hep8) bound to the positively charged RBD Patch site for (i) WT, (ii) Delta, and (iii) Omicron spike proteins. These images were generated by alignment with VMDtools.

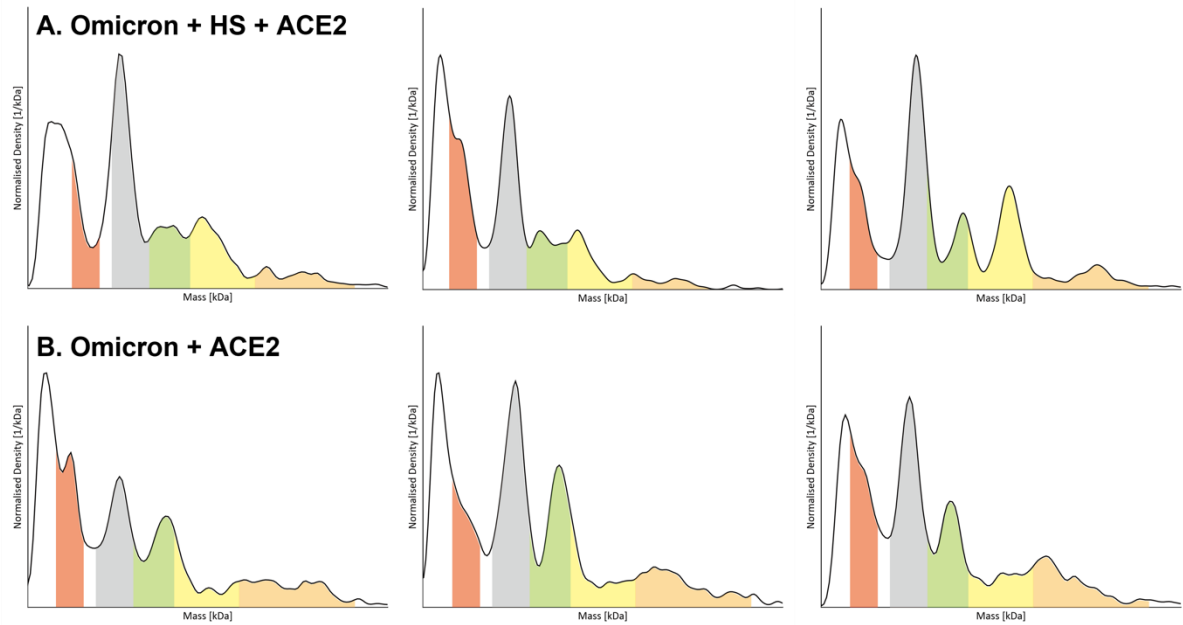


**Figure S14:** Repetition results of Omicron variant mass photometer. Row (A) Omicron spike + HS + ACE2, and row (B) Omicron spike + ACE2. Mass distribution of Omicron spike (mass range highlighted in grey), dACE2 (mass range highlighted in red), and Possible ternary complexes are grouped in A (green), B (yellow), C (orange) based on their expected mass ranges.

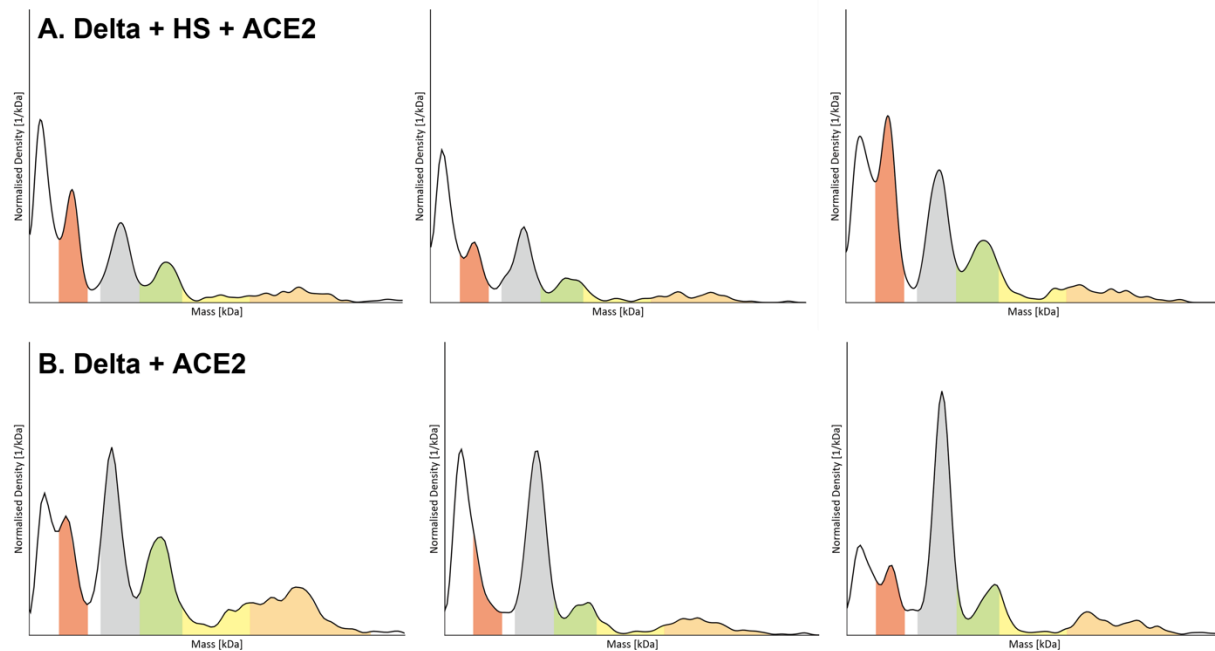


**Figure S15:** Repetition results of Delta variant mass photometer. Row (A) Delta spike + HS + ACE2, and row (B) Delta spike + ACE2. Mass distribution of Delta spike (mass range highlighted in grey), dACE2 (mass



range highlighted in red), and Possible ternary complexes are grouped in A (green), B (yellow), C (orange) based on their expected mass ranges.

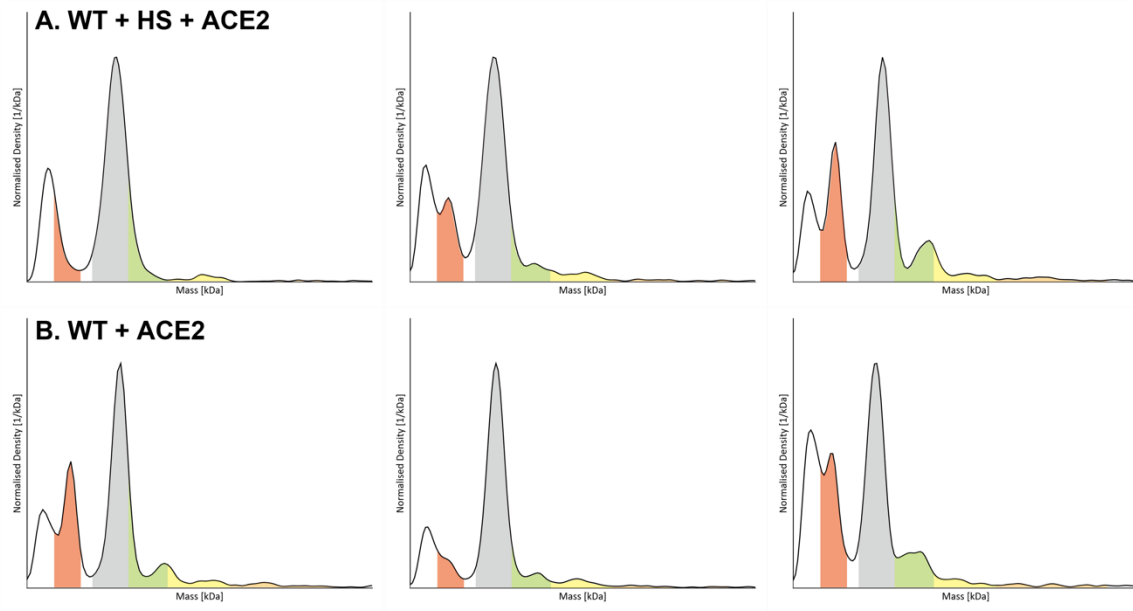


**Figure S16:** Repetition results of Wild type mass photometer. Row (A) WT spike + HS + ACE2, and row (B) WT spike + ACE2. Mass distribution of WT spike (mass range highlighted in grey), dACE2 (mass range highlighted in red), and Possible ternary complexes are grouped in A (green), B (yellow), C (orange) based on their expected mass ranges.

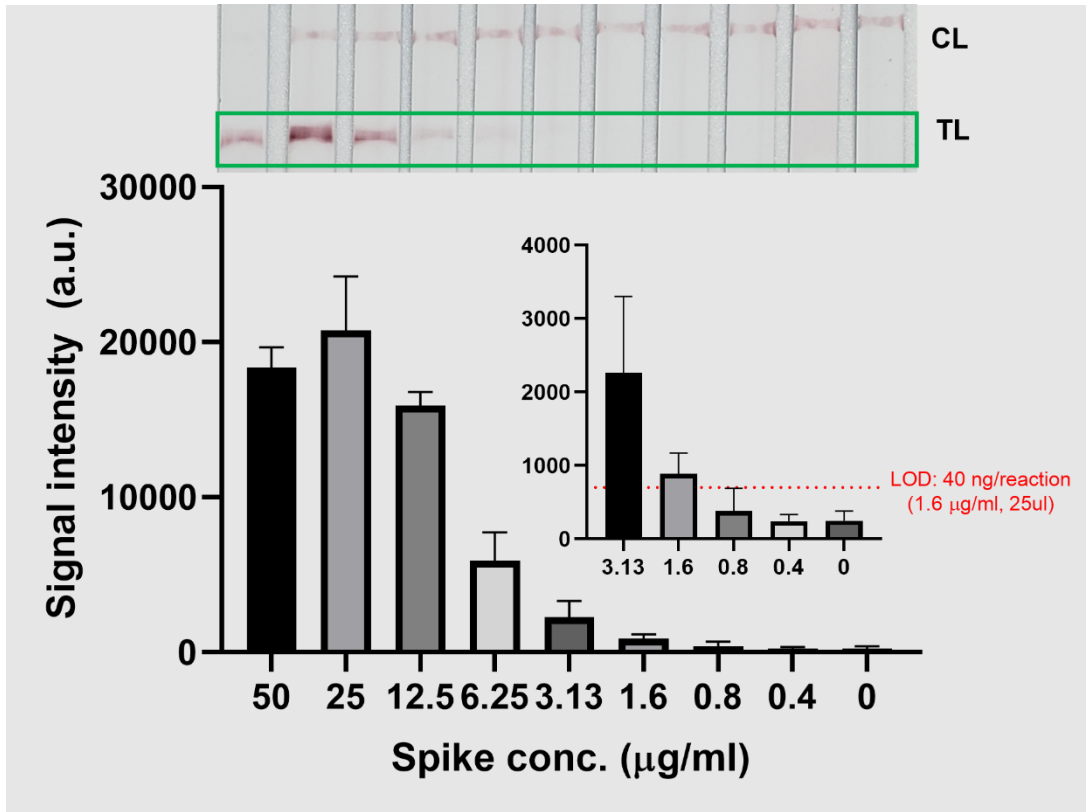


**Figure S17:** Dose-dependency results of Omicron detection using *GlycoGrip2.0* without signal enhancement in buffer condition. The limit of the detection was calculated by the blank + 3x (Standard deviation of blank). At least three independent tests were performed ( $n \geq 3$ ) for *Glycogrip*.

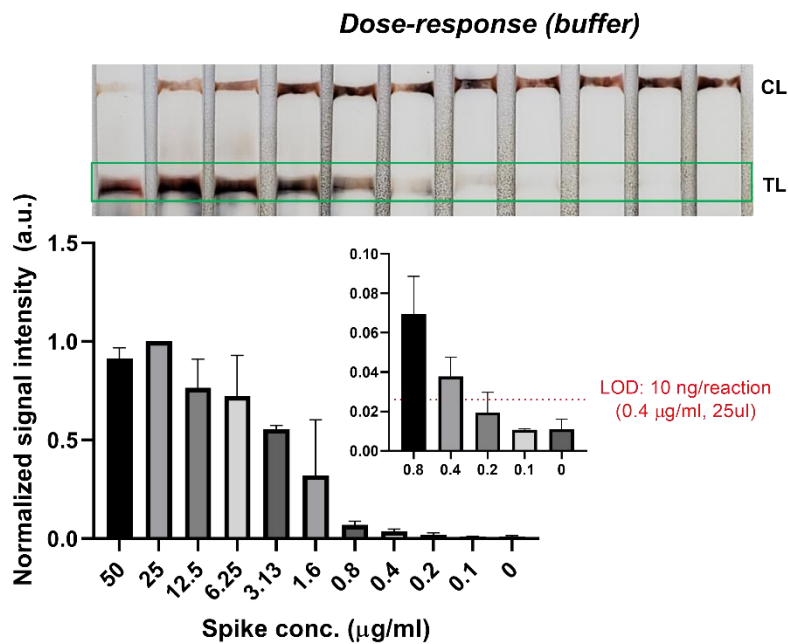




**Figure S18:** Dose-dependency results of Omicron detection using *GlycoGrip2.0* with signal enhancement in buffer condition. The limit of the detection was calculated by the blank + 3x (Standard deviation of blank). At least three independent tests were performed ( $n \geq 3$ ).

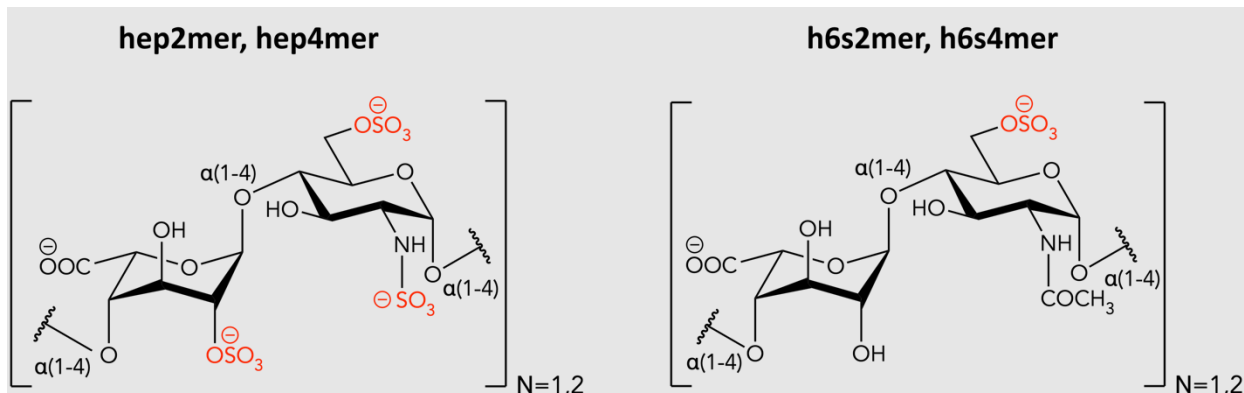


**Figure S19:** ChemDraws of all molecules modeled and docked in this work. Hep2mer, hep4mer, h6s2mer, h6s4mer.

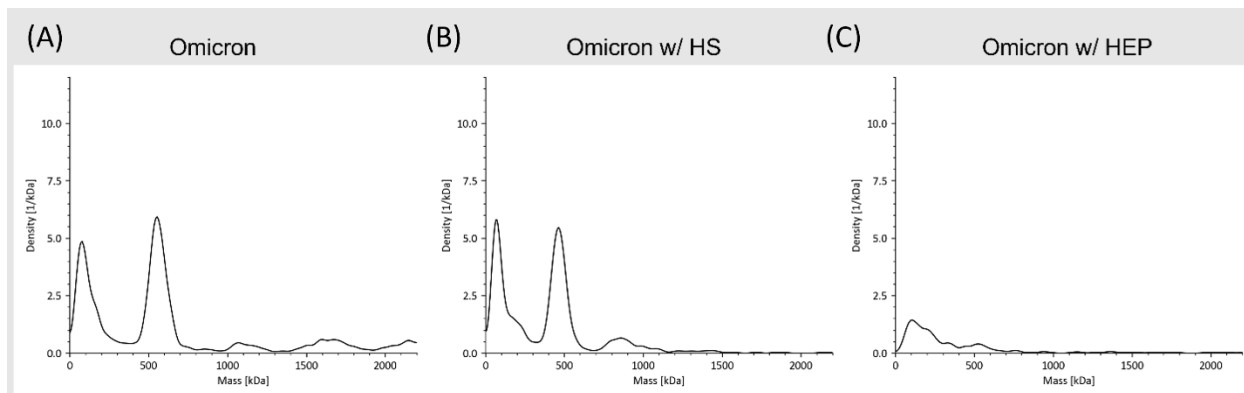


**Figure S20:** Comparison of the heparin and heparan sulfate for mass photometer. (A) Omicron spike only, (B) Omicron with heparan sulfate, (C) Omicron with heparin. The peak around 500 kDa represent the trimer spike protein. Count number for Omicron only sample at 500 kDa peak was 773, with heparan sulfate was 613, and with heparin was 68 counts.

## References:

1. Walls, A.C., Park, Y.-J., Tortorici, M.A., Wall, A., McGuire, A.T., and Velesler, D. (2020). Structure, Function, and Antigenicity of the SARS-CoV-2 Spike Glycoprotein. *Cell* 181, 281-292.e286. <https://doi.org/10.1016/j.cell.2020.02.058>.
2. Bangaru, S., Ozorowski, G., Turner, H.L., Antanasijevic, A., Huang, D., Wang, X., Torres, J.L., Diedrich, J.K., Tian, J.-H., Portnoff, A.D., et al. (2020). Structural analysis of full-length SARS-CoV-2 spike protein from an advanced vaccine candidate. *Science* 370, 1089-1094. 10.1126/science.abe1502.
3. Wrapp, D., Wang, N., Corbett, K.S., Goldsmith, J.A., Hsieh, C.-L., Abiona, O., Graham, B.S., and McLellan, J.S. (2020). Cryo-EM structure of the 2019-nCoV spike in the prefusion conformation. *Science* 367, 1260-1263. 10.1126/science.abb2507.
4. McCallum, M., Walls, A.C., Sprouse, K.R., Bowen, J.E., Rosen, L.E., Dang, H.V., De Marco, A., Franko, N., Tilles, S.W., Logue, J., et al. (2021). Molecular basis of immune evasion by the Delta and Kappa SARS-CoV-2 variants. *Science* 374, 1621-1626. 10.1126/science.abl8506.
5. Gobeil, S.M.C., Henderson, R., Stalls, V., Janowska, K., Huang, X., May, A., Speakman, M., Beaudoin, E., Manne, K., Li, D., et al. (2022). Structural diversity of the SARS-CoV-2 Omicron spike. *Molecular Cell* 82, 2050-2068.e2056. <https://doi.org/10.1016/j.molcel.2022.03.028>.
6. Tortorici, M.A., Beltramello, M., Lempp, F.A., Pinto, D., Dang, H.V., Rosen, L.E., McCallum, M., Bowen, J., Minola, A., Jaconi, S., et al. (2020). Ultrapotent human antibodies protect against SARS-CoV-2 challenge via multiple mechanisms. *Science* 370, 950-957. 10.1126/science.abe3354.
7. Casalino, L., Gaieb, Z., Goldsmith, J.A., Hjorth, C.K., Dommer, A.C., Harbison, A.M., Fogarty, C.A., Barros, E.P., Taylor, B.C., McLellan, J.S., et al. (2020). Beyond Shielding: The Roles of Glycans in the SARS-CoV-2 Spike Protein. *ACS Central Science* 6, 1722-1734. 10.1021/acscentsci.0c01056.
8. Watanabe, Y., Allen, J.D., Wrapp, D., McLellan, J.S., and Crispin, M. (2020). Site-specific glycan analysis of the SARS-CoV-2 spike. *Science* 369, 330-333. 10.1126/science.abb9983.
9. Olsson, M.H.M., Søndergaard, C.R., Rostkowski, M., and Jensen, J.H. (2011). PROPKA3: Consistent Treatment of Internal and Surface Residues in Empirical pKa Predictions. *Journal of Chemical Theory and Computation* 7, 525-537. 10.1021/ct100578z.
10. Schrödinger Release 2021-3. Protein Preparation Wizard. Schrödinger, LLC: New York, NY 2021.
11. Humphrey, W., Dalke, A., and Schulten, K. (1996). VMD: Visual molecular dynamics. *Journal of Molecular Graphics* 14, 33-38. [https://doi.org/10.1016/0263-7855\(96\)00018-5](https://doi.org/10.1016/0263-7855(96)00018-5).
12. Phillips, J.C., Braun, R., Wang, W., Gumbart, J., Tajkhorshid, E., Villa, E., Chipot, C., Skeel, R.D., Kalé, L., and Schulten, K. (2005). Scalable molecular dynamics with NAMD. *Journal of Computational Chemistry* 26, 1781-1802. <https://doi.org/10.1002/jcc.20289>.
13. Phillips, J.C., Hardy, D.J., Maia, J.D.C., Stone, J.E., Ribeiro, J.V., Bernardi, R.C., Buch, R., Fiorin, G., Hénin, J., Jiang, W., et al. (2020). Scalable molecular dynamics on CPU and GPU architectures with NAMD. *The Journal of Chemical Physics* 153, 044130. 10.1063/5.0014475.
14. Huang, J., and MacKerell Jr, A.D. (2013). CHARMM36 all-atom additive protein force field: Validation based on comparison to NMR data. *Journal of Computational Chemistry* 34, 2135-2145. <https://doi.org/10.1002/jcc.23354>.
15. Huang, J., Rauscher, S., Nawrocki, G., Ran, T., Feig, M., de Groot, B.L., Grubmüller, H., and MacKerell, A.D. (2017). CHARMM36m: an improved force field for folded and intrinsically disordered proteins. *Nature Methods* 14, 71-73. 10.1038/nmeth.4067.
16. Guvench, O., Hatcher, E., Venable, R.M., Pastor, R.W., and MacKerell, A.D., Jr. (2009). CHARMM Additive All-Atom Force Field for Glycosidic Linkages between Hexopyranoses. *Journal of Chemical Theory and Computation* 5, 2353-2370. 10.1021/ct900242e.

17. Trott, O., and Olson, A.J. (2010). AutoDock Vina: Improving the speed and accuracy of docking with a new scoring function, efficient optimization, and multithreading. *Journal of Computational Chemistry* *31*, 455-461. <https://doi.org/10.1002/jcc.21334>.
18. Morris, G.M., Huey, R., Lindstrom, W., Sanner, M.F., Belew, R.K., Goodsell, D.S., and Olson, A.J. (2009). AutoDock4 and AutoDockTools4: Automated docking with selective receptor flexibility. *Journal of Computational Chemistry* *30*, 2785-2791. <https://doi.org/10.1002/jcc.21256>.
19. Michaud-Agrawal, N., Denning, E.J., Woolf, T.B., and Beckstein, O. (2011). MDAAnalysis: A toolkit for the analysis of molecular dynamics simulations. *Journal of Computational Chemistry* *32*, 2319-2327. <https://doi.org/10.1002/jcc.21787>.
20. Richard J. Gowers, M.L., Jonathan Barnoud, Tyler J. E. Reddy, Manuel N. Melo, Sean L. Seyler, Jan Domański, David L. Dotson, Sébastien Buchoux, Ian M. Kenney, Oliver Beckstein (2016). MDAAnalysis: A Python Package for the Rapid Analysis of Molecular Dynamics Simulations. pp. 98–105.
21. Fabian Pedregosa, G.V., Alexandre Gramfort, Vincent Michel, Bertrand Thirion, Olivier Grisel, Mathieu Blondel, Peter Prettenhofer, Ron Weiss, Vincent Dubourg, Jake Vanderplas, Alexandre Passos, David Cournapeau, Matthieu Brucher, Matthieu Perrot, Édouard Duchesnay (2011). Scikit-learn: Machine Learning in Python. *Journal of Machine Learning Research* *12*, 2825-2830.
22. Kim, S.H., Kearns, F.L., Rosenfeld, M.A., Casalino, L., Papanikolas, M.J., Simmerling, C., Amaro, R.E., and Freeman, R. (2022). GlycoGrip: Cell Surface-Inspired Universal Sensor for Betacoronaviruses. *ACS Central Science* *8*, 22-42. 10.1021/acscentsci.1c01080.
23. Shrake, A., and Rupley, J.A. (1973). Environment and exposure to solvent of protein atoms. Lysozyme and insulin. *Journal of Molecular Biology* *79*, 351-371. [https://doi.org/10.1016/0022-2836\(73\)90011-9](https://doi.org/10.1016/0022-2836(73)90011-9).
24. Schrödinger Release 2022-3. Induced Fit Docking Protocol. Schrödinger, LLC: New York, NY 2022.
25. Lu, C., Wu, C., Ghoreishi, D., Chen, W., Wang, L., Damm, W., Ross, G.A., Dahlgren, M.K., Russell, E., Von Bargen, C.D., et al. (2021). OPLS4: Improving Force Field Accuracy on Challenging Regimes of Chemical Space. *Journal of Chemical Theory and Computation* *17*, 4291-4300. 10.1021/acs.jctc.1c00302.
26. Schrödinger Release 2021-3. LigPrep. Schrödinger, LLC: New York, NY 2021.
27. Dolinsky, T.J., Nielsen, J.E., McCammon, J.A., and Baker, N.A. (2004). PDB2PQR: an automated pipeline for the setup of Poisson–Boltzmann electrostatics calculations. *Nucleic Acids Research* *32*, W665-W667. 10.1093/nar/gkh381.
28. Dolinsky, T.J., Czodrowski, P., Li, H., Nielsen, J.E., Jensen, J.H., Klebe, G., and Baker, N.A. (2007). PDB2PQR: expanding and upgrading automated preparation of biomolecular structures for molecular simulations. *Nucleic Acids Research* *35*, W522-W525. 10.1093/nar/gkm276.
29. Huber, G.A., and McCammon, J.A. (2010). Browndye: A software package for Brownian dynamics. *Computer Physics Communications* *181*, 1896-1905. <https://doi.org/10.1016/j.cpc.2010.07.022>.
30. Huber, G.A., and McCammon, J.A. (2019). Brownian Dynamics Simulations of Biological Molecules. *Trends in Chemistry* *1*, 727-738. <https://doi.org/10.1016/j.trechm.2019.07.008>.
31. Jurrus, E., Engel, D., Star, K., Monson, K., Brandi, J., Felberg, L.E., Brookes, D.H., Wilson, L., Chen, J., Liles, K., et al. (2018). Improvements to the APBS biomolecular solvation software suite. *Protein Science* *27*, 112-128. <https://doi.org/10.1002/pro.3280>.
32. Baker, N.A., Sept, D., Joseph, S., Holst, M.J., and McCammon, J.A. (2001). Electrostatics of nanosystems: Application to microtubules and the ribosome. *Proc National Acad Sci* *98*, 10037-10041. 10.1073/pnas.181342398.
33. Holst, M. (2001). Adaptive Numerical Treatment of Elliptic Systems on Manifolds. *Advances in Computational Mathematics* *15*, 139-191. 10.1023/A:1014246117321.

34. Holst, M.J., and Saied, F. (1995). Numerical solution of the nonlinear Poisson–Boltzmann equation: Developing more robust and efficient methods. *Journal of Computational Chemistry* *16*, 337-364. <https://doi.org/10.1002/jcc.540160308>.
35. Bank, R.E., and Holst, M. (2003). A New Paradigm for Parallel Adaptive Meshing Algorithms. *SIAM Review* *45*, 291-323. 10.1137/S003614450342061.
36. Holst, M., and Saied, F. (1993). Multigrid solution of the Poisson—Boltzmann equation. *Journal of Computational Chemistry* *14*, 105-113. <https://doi.org/10.1002/jcc.540140114>.
37. Chavanis, P.-H. (2019). The Generalized Stochastic Smoluchowski Equation. *Entropy* *21*. 10.3390/e21101006.
38. Votapka, L.W., and Amaro, R.E. (2015). Multiscale Estimation of Binding Kinetics Using Brownian Dynamics, Molecular Dynamics and Milestoning. *PLOS Computational Biology* *11*, e1004381. 10.1371/journal.pcbi.1004381.
39. Yan, R., Zhang, Y., Li, Y., Xia, L., Guo, Y., and Zhou, Q. (2020). Structural basis for the recognition of SARS-CoV-2 by full-length human ACE2. *Science* *367*, 1444-1448. 10.1126/science.abb2762.
40. Barros, E.P., Casalino, L., Gaieb, Z., Dommer, A.C., Wang, Y., Fallon, L., Raguette, L., Belfon, K., Simmerling, C., and Amaro, R.E. (2021). The flexibility of ACE2 in the context of SARS-CoV-2 infection. *Biophysical Journal* *120*, 1072-1084. <https://doi.org/10.1016/j.bpj.2020.10.036>.
41. Panferov, V.G., Safenkova, I.V., Varitsev, Y.A., Drenova, N.V., Kornev, K.P., Zherdev, A.V., and Dzantiev, B.B. (2016). Development of the sensitive lateral flow immunoassay with silver enhancement for the detection of *Ralstonia solanacearum* in potato tubers. *Talanta* *152*, 521-530. <https://doi.org/10.1016/j.talanta.2016.02.050>.
42. Lee, J.-H., Choi, M., Jung, Y., Lee, S.K., Lee, C.-S., Kim, J., Kim, J., Kim, N.H., Kim, B.-T., and Kim, H.G. (2021). A novel rapid detection for SARS-CoV-2 spike 1 antigens using human angiotensin converting enzyme 2 (ACE2). *Biosensors and Bioelectronics* *171*, 112715. <https://doi.org/10.1016/j.bios.2020.112715>.
43. Baker, A.N., Richards, S.-J., Guy, C.S., Congdon, T.R., Hasan, M., Zwetsloot, A.J., Gallo, A., Lewandowski, J.R., Stansfeld, P.J., Straube, A., et al. (2020). The SARS-COV-2 Spike Protein Binds Sialic Acids and Enables Rapid Detection in a Lateral Flow Point of Care Diagnostic Device. *ACS Central Science* *6*, 2046-2052. 10.1021/acscentsci.0c00855.
44. Lee, J.-H., Lee, Y., Lee, S.K., Kim, J., Lee, C.-S., Kim, N.H., and Kim, H.G. (2022). Versatile role of ACE2-based biosensors for detection of SARS-CoV-2 variants and neutralizing antibodies. *Biosensors and Bioelectronics* *203*, 114034. <https://doi.org/10.1016/j.bios.2022.114034>.